

---

CHAPTER  
**TWO**

---

## THE EXPERIMENTAL APPARATUS

The “Large Hadron Collider” (LHC) accelerator and the “Compact Muon Solenoid” (CMS) detector, situated across Swiss-French border in Geneva, Switzerland at the European Organization of Nuclear Research (CERN), has been used to accumulate data for this study. This chapter presents a brief introduction and description of the design and performance of these accelerator and detector facilities.

### 2.1 The Large Hadron Collider

The Big-Bang theory [98] provides an explanation of the origin of the universe. It says that the universe initially started from a small singularity and an explosion (called Big-Bang) put the universe into a continuous state of inflation, so it took around 13.7 billion years for the universe to reach in the present state (Fig. 2.1). During the initial seconds after the birth of universe, the temperature was tremendously high and the universe consists of plasma of vast number of fundamental particles interacting with each other with extremely high energies. In order to study the properties of early universe, scientists use particle accelerators in which sub-atomic particles travelling at relativistic speeds are made to undergo inelastic collisions to reproduce the conditions that existed at the time of Big-Bang or soon there after.

The Large Hadron Collider [99, 100] as the name suggests is a large circular

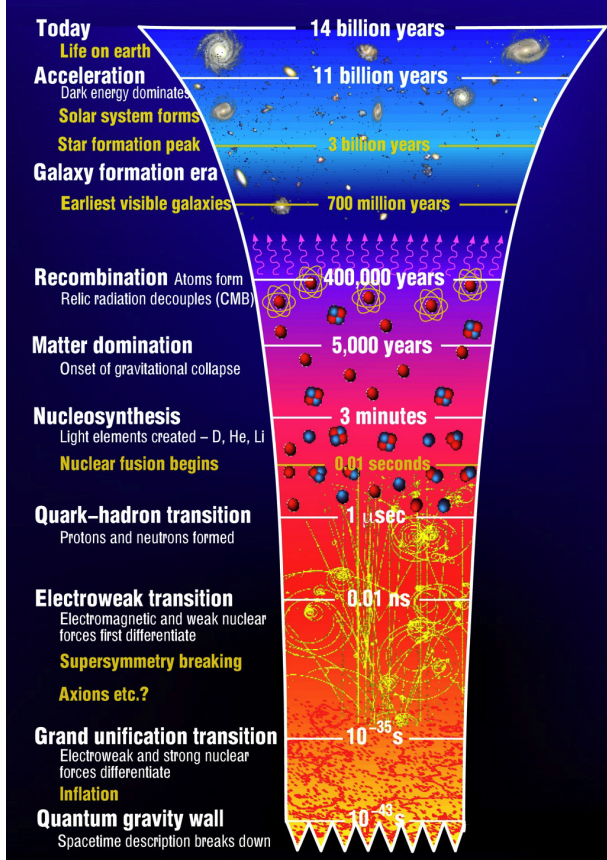


Figure 2.1: Big-Bang timeline.

accelerator having a circumference of  $\sim 27$  km which accelerates counter rotating beams of hadrons and collides them to study the fundamental properties and interactions of quarks, leptons and bosons. It is the world's largest and most complex particle accelerator ever built. Earlier particle accelerators like "Large Electron Positron" collider (LEP) [101] at CERN (in the same tunnel where LHC has been built) and Tevatron [102] at Fermilab, Batavia, IL, USA, have been extensively used to confirm the predictions and test the precision of Standard Model parameters. Both of these were circular colliders. The LEP was an  $e^+e^-$  collider with a center of mass energy ( $\sqrt{s}$ ) ranging from 90 GeV to 209 GeV while Tevatron was a  $p\bar{p}$  collider with  $\sqrt{s} = 1.8$  TeV and 1.96 TeV. Studying a collision data obtained from electron-positron beam is far more easier as compared to proton beams due to the absence of hadronic background in the former. However, in a circular ring of a particular radius, the loss of energy caused by synchrotron radiations is given as:

$$-\Delta E = \frac{4\pi\alpha}{3r}\beta^3\gamma^4 \quad (\beta = v/c \approx 1 \text{ and } \gamma = E/mc^2 \text{ for relativistic speeds}), \quad (2.1)$$

which is very large due to small mass of  $e^+$  and  $e^-$  and further increases as the speed  $v$  approaches the speed of light  $c$ . The choice is to either increase the radius of the circular rings or to use linear colliders or use heavy particles in collision beams. The first two instances are not very easy to meet either due to technical or financial constraints, so in order to achieve very high energies, proton beams are used. Since  $m_p \simeq 2000 m_e$ , use of proton beam reduces synchrotron losses by a factor of  $(2000)^4 \simeq 10^{13}$ .

The requirement of very high energies for particle accelerators can be explained by the fact that in scattering experiments, the wavelength of the probe should be smaller than the target particle size in order to observe the particle. Since, in particle physics, we look for extraordinarily small entities, we need probes of smaller wavelengths or higher energies (as per the de broglie's relation,  $\lambda = \frac{h}{mv}$ ).

### 2.1.1 LHC tunnel layout

The LHC is situated in an underground tunnel having a circumference of 26.7 km and a diameter of 3.8 m at a depth of around 45 to 170 m beneath the France-Switzerland border. The LHC tunnel is divided in eight straight sections, each of 528 m separated by eight arcs. The straight sections are utilized as experimental or utility insertions. A schematic diagram representing the layout of LHC tunnel is shown in Fig. 2.2.

The eight sections are numbered from 1 to 8. The two general purpose detectors, namely, A Toroidal LHC Apparatus (ATLAS) [103] and Compact Muon Solenoid (CMS) [104] are located at point 1 and point 5 respectively. Point 2 is occupied by the heavy ion detector, A Large Ion Collider Experiment (ALICE) [105] while the detector for b-physics study, Large Hadron Collider beauty (LHCb) [106] is placed at point 8. These two points also have the beam injection utility for the two beams. Collimation systems utilized for beam cleaning are placed at point 3 and 7 while the radio frequency (RF) systems for each beam are present at point 4. The point 6 has been used for the beam dump where the two beams are extracted vertically using horizontally and vertically deflecting magnets. The LHC is primarily a proton-proton collider, but it also uses heavy ion beams to perform proton-lead and lead-lead collisions for some short periods of time.

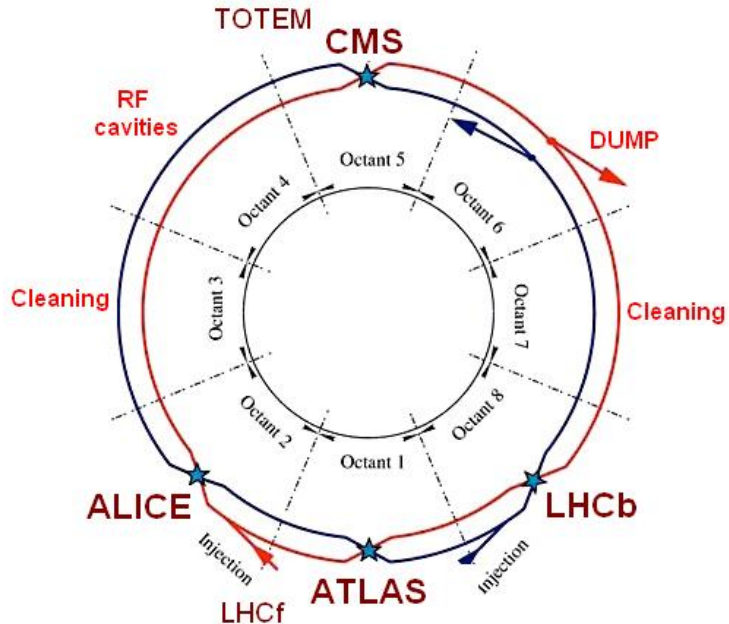


Figure 2.2: A schematic layout of the LHC tunnel.

### 2.1.2 Main components of the LHC

The design of LHC depends on very basic physics principles associated with latest technology. The three main components of LHC are:

- 1. Radio Frequency (RF) cavities:** The RF cavities are located along the beam pipe and are used to provide acceleration to the proton beams using alternating electric field. There are two independent RF systems, one for each beam. A sketch of a RF cavity is shown in the Fig. 2.3 below.

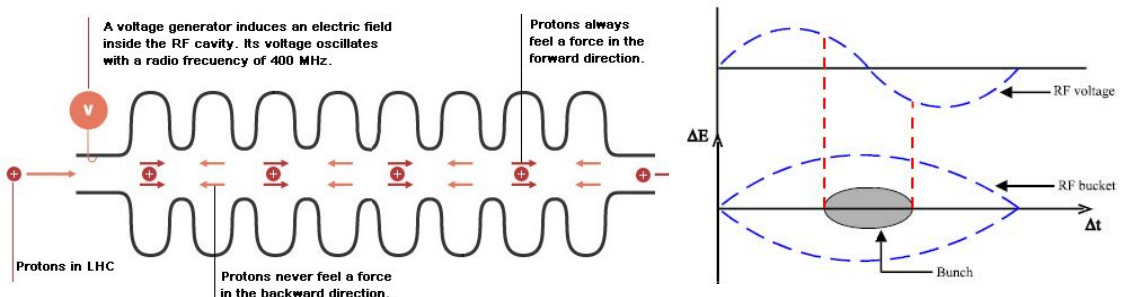


Figure 2.3: A Radio Frequency cavity.

Figure 2.4: A sketch showing formation of a bunch.

The sinusoidal varying alternating electric field of RF cavity changes polarity after each half cycle which implies that it accelerates the protons during one half cycle and decelerates during the other half. This results into the formation of bunches of protons. As can be seen in Fig. 2.4, when a proton arrives inside

a RF cavity at a time when the voltage is zero, it will see no force and is called synchronous proton. Any proton arriving before the synchronous proton will see a negative polarity and hence will decelerate while any proton arriving later than the synchronous proton will see positive polarity and will get accelerated, so these protons will come closer to the synchronous proton and form a bunch. At LHC, the RF cavities resonate at a frequency of 400 MHz. The LHC is designed to have a total of 2808 bunches at a gap of 25 ns. The main goal of RF cavities is to maintain the tightness of proton bunches to provide high luminosity at collision points. These cavities also transfer the radio frequency power to the beam to provide acceleration. The LHC has eight RF cavities per beam operating at  $4.5^{\circ}$  K, each delivering a power of 2 MV at 400 MHz.

2. **Vacuum chamber:** The beam pipe in which proton beams travel are kept at a low pressure of  $\sim 10^{-13}$  bar, much less than the outer space, forming an ultrahigh vacuum. This is required to minimize the interactions with parasitic particles and subsequent loss of accelerated protons.
3. **Magnet system:** In order to provide proper bending and focusing of the proton beams, an intense magnetic field varying in the range of 0.54 T (for 450 GeV proton energy) to 8.33 T (for 7 TeV proton energy) has been used. This high magnetic field has been achieved by the use of superconducting magnets made of copper plated Niobium-Titanium (NbTi) superconductors. The superconducting state has been attained by using many tones of superfluid Helium cooled to a temperature of  $1.9^{\circ}$  K. Due to the constraints of small tunnel diameter, it was not possible to make completely separate rings for both the proton beams. So an alternate way was adopted in the form of twin-bore magnet design (a front view is shown in Fig. 2.5) which comprises of two coils and beam pipes at a separation of 180 mm within the same mechanical framework. This magnet structure is constructed in such a way that it provides opposite magnetic fields in the two beam pipes. The copper plated NbTi filaments are joined together to make the cables and two layers of these cables are wrapped around each beam pipe. The current is made to flow in opposite directions through the cables around the two pipes, which produces an intense magnetic field of opposite polarity in both the beam pipes. The copper provides an insulation among the NbTi filaments in superconducting state and act as a conductor upon reaching the conducting state.

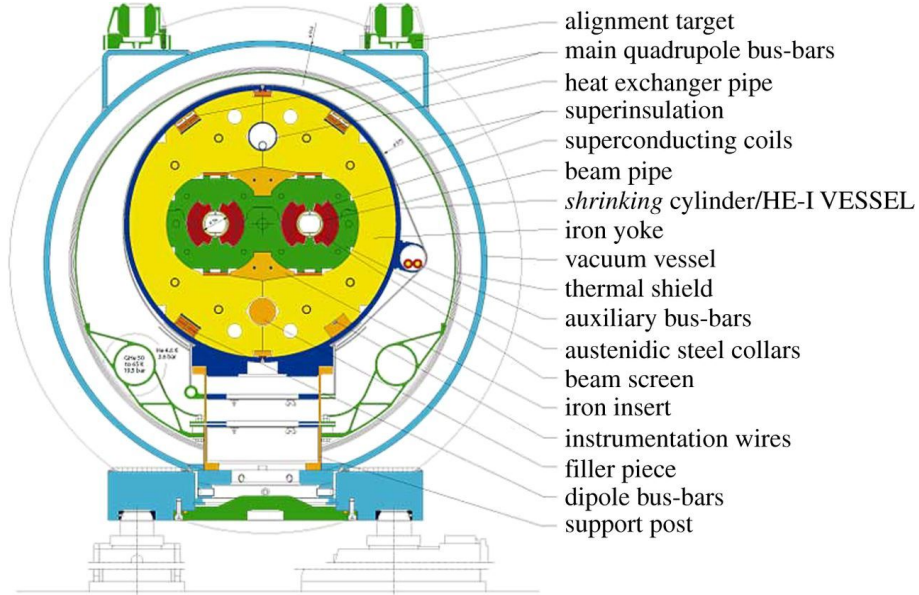


Figure 2.5: The LHC twin-bore magnet system

The LHC consists of different type of magnets that include, dipoles used for bending of the particle's beam, quadrupoles used for focusing of the beam, sextupoles and octupoles used for correcting the size and position of the beam. The LHC ring consists of 1232 dipoles, 392 quadrupoles and many sextupoles and octupoles. To enhance the probability of collisions, the bunches are squeezed by the use of special magnets positioned near the collision chambers. These magnets reduce the beam diameter to a minimum of  $16 \mu\text{m}$ .

### 2.1.3 Proton's journey to maximum acceleration

Making the proton beams travel closer to the speed of light is a very intricate task. At LHC, it has been accomplished in a number of steps as can be seen in the schematic representation of CERN accelerator complex [107] in Fig. 2.6. First of all, protons are extracted from hydrogen gas by stripping off the electrons using an electric discharge. Then, the protons are directed towards a Radio Frequency Quadrupole (QRF) that provides an initial acceleration of 750 keV to the beam. After that, the protons are sent to LINAC2, a linear accelerator that makes use of RF cavities and accelerates the proton beam upto 50 MeV. The beam from LINAC2 is made to enter Proton Synchrotron Booster (PSB) which increases the energy of protons to 1.4 GeV and divides the proton beam into 6 bunches. The output of PSB is then injected into Proton Synchrotron (PS) that accelerates the protons upto 25 GeV. The PS is also responsible for preparing the LHC bunch

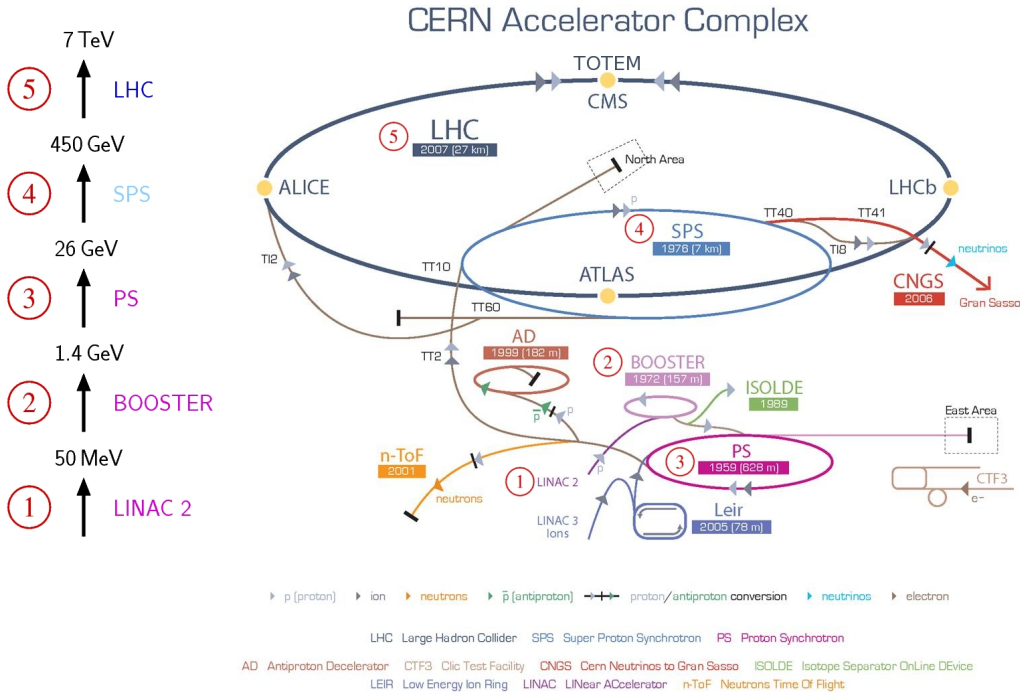


Figure 2.6: A schematic view of CERN accelerator complex representing the different accelerators deployed for providing acceleration to the proton beam.

structure. A total of 72 bunches with a spacing of 25 ns are formed in PS. The proton bunches from PS then enter into Super Proton Synchrotron (SPS) where they are further bunched into 288 bunches and are accelerated upto the LHC injection energy of 450 GeV. The protons from SPS are then finally made to enter into LHC where they accelerated upto the highest energy required.

### 2.1.4 Luminosity measurements at LHC

At LHC, the rate of collision  $N$  is expressed in terms of the instantaneous luminosity  $L$  as  $N = \sigma L$  where  $\sigma$  is the cross section of the process under study. For a given process, the higher the luminosity, the chances are more of a collision to happen. The luminosity of a beam depends upon many machine parameters and is given by,

$$L = \frac{N_b^2 n_b f_{rev} \gamma_r}{4\pi \beta^* \epsilon_n} F, \quad (2.2)$$

where,

$N_b$ : number of particles in a bunch,

$n_b$ : number of bunches in each beam,

$f_{rev}$ : beam revolution frequency,

$\gamma_r$ : relativistic gamma factor,

$\epsilon_n$ : normalized transverse beam emittance<sup>1</sup>,

$\beta^*$ : betatron function<sup>2</sup>, and

$F$ : luminosity reduction factor due to the presence of crossing angle between the two beams.

In order to achieve highly luminous beams, one need to provide large number of highly populated bunches having low value of beam emittance and betatron function colliding at high frequencies. The various parameters related to LHC machine and proton beams are summarized in Table 2.1.

| LHC Parameters   | Design Value         | 2016 Value           |
|--|----------------------|----------------------|
| Total number of magnets                                      | 9600                 | —                    |
| Number of dipole magnets                                     | 1232                 | —                    |
| Beam energy (TeV)  | 14                   | 13                   |
| Bunch spacing (ns)   | 25                   | 25                   |
| No. of protons per bunch                                     | $1.1 \times 10^{11}$ | $1.1 \times 10^{11}$ |
| No. of bunches per beam                                      | 2808                 | 2220                 |
| Beam crossing angle ( $\mu\text{rad}$ )                      | 285                  | 370                  |
| Beam emittance, $\epsilon_n$ ( $\mu\text{m}$ )               | 3.75                 | 3.4                  |
| Betatron function, $\beta^*$ (m)                             | 0.55                 | 0.4                  |
| Instantaneous luminosity ( $\text{cm}^{-2}\text{sec}^{-1}$ ) | $1.0 \times 10^{34}$ | $1.0 \times 10^{34}$ |

Table 2.1: Design values of the various parameters of LHC and a comparison with the values obtained during the 2016 run.

The sum of instantaneous luminosities obtained over a period of time is referred to as the integrated luminosity. The Fig. 2.7 shows the total integrated luminosity delivered by the LHC and recorded by CMS [108] over a period of time for the year 2016.

During the 13 TeV run in 2016, the LHC delivered a total of  $40.8 \text{ fb}^{-1}$  of pp collision data, out of which, CMS recorded a total of  $37.8 \text{ fb}^{-1}$ . The CMS has certified  $35.9 \text{ fb}^{-1}$  of recorded data to be used for physics analysis. The study presented in this thesis has been performed using this  $35.9 \text{ fb}^{-1}$  of data.

---

<sup>1</sup>The beam emittance is defined as the transverse size of the beam. The narrower the beam, the lesser is the beam emittance and more are the chances of interaction.

<sup>2</sup>Betatron function is defined as the distance from the collision point at which the beam width in transverse plane is twice compared to the beam width at collision point.

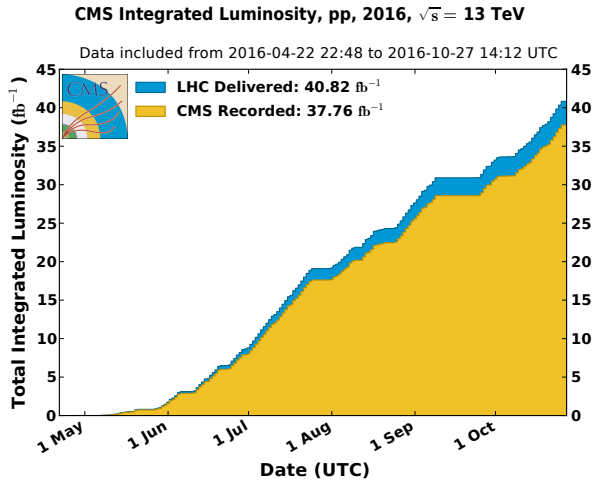


Figure 2.7: Total integrated luminosity delivered by the LHC and recorded by CMS as a function of time, during the year 2016 [108].

## 2.2 The CMS Detector

The CMS detector [109] is one of the main particle detectors designed at the LHC to observe different kind of particles and processes produced in the pp collisions. The prime objective of the CMS detector is to explore the physics at Terascale, the energy region at which the physicists believe the experiment has the potential to answer some of the existing key questions. The detector has a cylindrical onion like structure having a coverage of  $4\pi$  steradian, with each layer representing a different sub-detector used to measure different type of particles. The information from different layers is used to build up the complete picture of an event. It is situated in a cavern, 100 m underground, located at point 5 of the LHC tunnel in France near village Cessy. It has a length of 21.6 m and a diameter of 14.6 m, it weights around 14,000 tonnes. CMS is a large scientific collaboration involving around 3,000 people from 198 scientific institutions and universities belonging to 45 countries.

**Experimental challenges:** As discussed in last section, the LHC has a very high collision rate which is achieved by colliding bunches of more than 100 billion protons each, 40 million times every second, resulting into a pp interaction rate of around  $10^9$  per second. The high track density arising due to these interactions create severe radiation environment. The detector needs to remain unaffected from these radiations along with providing efficient particle identification. The detector has to face the challenge of adjusting between occupancy and granularity. Additionally, a

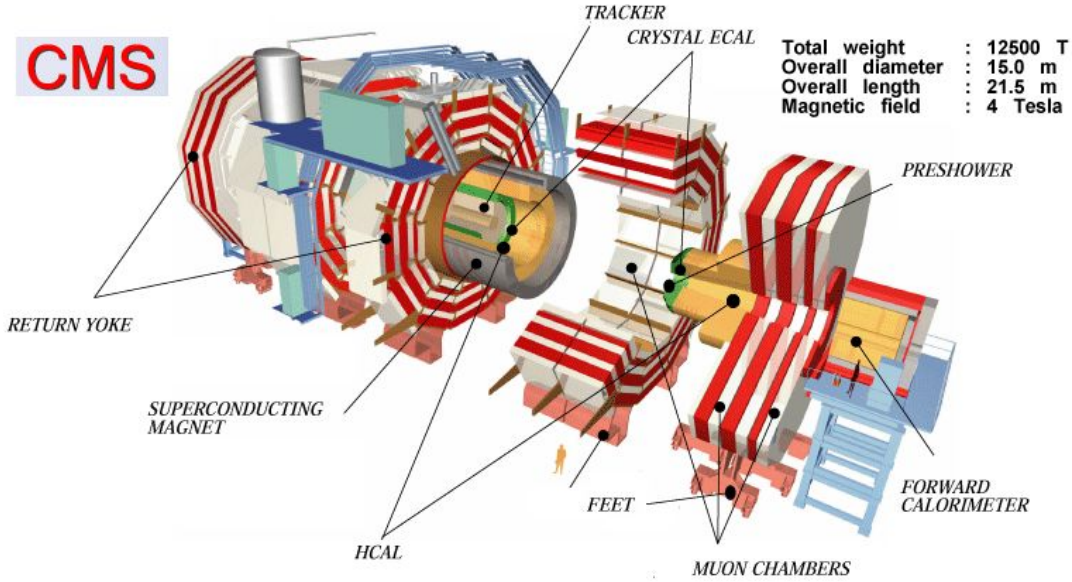


Figure 2.8: A layout of the CMS experiment at CERN.

majority of collisions contain uninteresting events, a fast filtering trigger system is required to reject these unwanted events. Also, the interesting pp events are superimposed by many uninteresting events occurring in the same bunch crossing (known as pile-up). Dealing with these events require high granularity and good time resolution detectors, which further demand to have large number of detector channels with good synchronization. Even storing the data after huge reduction require about 10 million gigabytes per year which in itself is a big challenge.

### 2.2.1 Layout of the CMS detector

A general layout of the CMS detector is presented in Fig. 2.8. It is based on four principle sub-systems: A high granularity central tracker, a homogeneous electromagnetic calorimeter, a sampling hadron calorimeter and a muon detector. The heart of the CMS is its very high superconducting magnet that is situated between the calorimeters and the muon detector. All the sub-systems of the detector are divided into one cylindrical barrel region and two opposite facing endcap regions, complimented with very forward regions. This arrangement provides a very good coverage of the collision fragments required for event building. A longitudinal view of the CMS detector system, showing the barrel and endcap sections of various sub-detectors is presented in Fig. 2.9, with the origin denoting the interaction point.

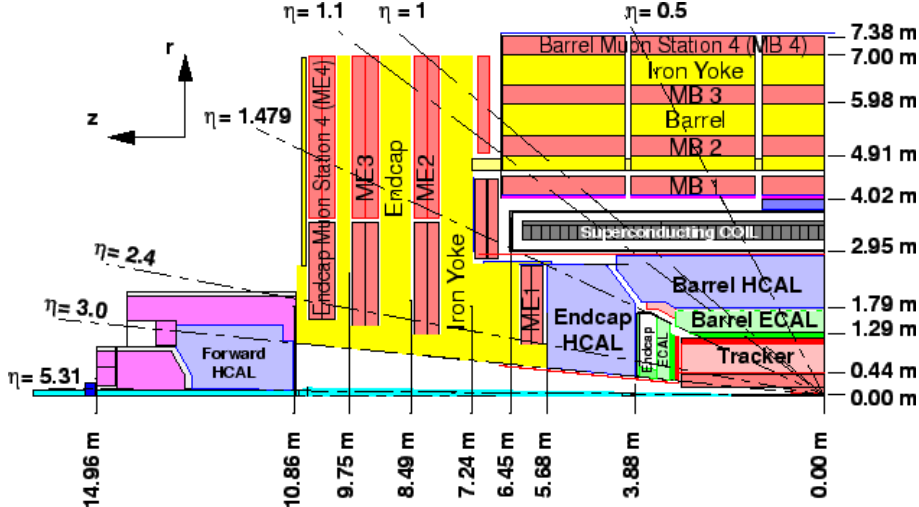


Figure 2.9: Longitudinal contour of a quadrant of the CMS detector.

**Co-ordinate system:** The CMS has adopted a right-handed spherical co-ordinate system with origin at the center of the detector which is also the intended collision point. The  $x$ -axis points towards the center of the LHC tunnel, the  $y$ -axis is vertically upwards and the  $z$ -axis is along the beam pipe. The polar angle  $\theta$  is taken from the  $z$ -axis to the  $x$ - $y$  plane and the azimuthal angle  $\phi$  is taken from the  $x$ -axis to the  $y$ -axis in the  $x$ - $y$  plane. The angle  $\theta$  denotes the particle's angle w.r.t the beam axis while angle  $\phi$  denotes the particle's orientation in the transverse plane. The co-ordinate  $r$  denotes the radial distance and is defined by  $r = \sqrt{x^2 + y^2 + z^2}$ . It is conventional to use pseudorapidity  $\eta$  instead of polar angle  $\theta$  as seen in Fig. 2.9. The pseudorapidity is defined in terms of angle  $\theta$  as

$$\eta = -\ln \left[ \tan \frac{\theta}{2} \right]. \quad (2.3)$$

On going from  $-z$  to  $+z$  axis,  $\theta$  goes from  $-\pi$  to  $+\pi$  and  $\eta$  goes from  $-\infty$  to  $+\infty$ . In the non-relativistic limit, it is called rapidity and is defined as,

$$y = \frac{1}{2} \ln \left( \frac{E + p_z}{E - p_z} \right), \quad (2.4)$$

where  $E$  and  $p_z$  are the particle's energy and  $z$ -component of the momentum. The rapidity,  $y$  requires the measurement of both  $E$  and  $p_z$  and in relativistic regime, it is quite difficult to measure the  $z$ -component of momentum very precisely. The reason of choosing  $\eta$  over  $\theta$  is that the difference between the pseudorapidity of two particles ( $\Delta\eta$ ) is Lorentz invariant under boosts along the beam axis. This means that an observer in the lab frame, boosted along  $z$ -axis w.r.t the rest frame, will

measure the same  $\Delta\eta$  between two particles as an observer in the rest frame. The importance of this feature comes from the fact that in the pp collisions, the hard interaction takes place between proton constituents (quarks or gluons), usually having different momenta, which means the different interactions have different boosts of their center-of-mass frames w.r.t the detector rest frame. Invariance of  $\Delta\eta$  under boosts allows us to treat the different interactions in a similar way as the interaction happening in the center-of-mass rest frame. The various histograms binned on the angular separation of particles will remain undistorted by these arbitrary boosts of different events. The angular distance  $R$  between two particles in  $\eta - \phi$  plane, as observed from the origin of CMS detector, is written in terms of the differences in  $\eta$  and  $\phi$  as,  $R = \sqrt{(\Delta\eta)^2 + (\Delta\phi)^2}$ .

In colliders, two particle beams colliding head-on consist of only longitudinal component of momentum. So the particles in the beam do not have a transverse component of momentum before collision, thus by conservation of momentum, the total transverse momentum after the collision should also add up to zero. This feature is extensively used in collider experiments and it requires to consider the particle's energy and momentum in the transverse direction, known as transverse energy ( $E_T$ ) and transverse momentum ( $p_T$ ), defined as  $E_T = E \sin\theta$  and  $p_T = \sqrt{p_x^2 + p_y^2}$  respectively. Any imbalance in the transverse momentum is caused by either the invisible particles like neutrinos or by the energy lost in the unavoidable nuclear processes. This imbalance is known as missing transverse energy and is given by,  $E_T^{\text{miss}} = -\sum p_T$ .

A short description of all the components of the CMS detector from innermost to outermost has been provided as follows:

### 2.2.1.1 CMS tracking system

The tracker [109, 110] is the innermost sub-detector, installed close to the interaction point. It has been designed to build tracks of charged particles coming out of the collisions and reconstruct primary as well as secondary vertices, with utmost precision and accuracy.

The tracker has a total length of 5.8 m, a diameter of 2.5 m and covers a region upto  $|\eta| < 2.5$ . A uniform magnetic field of 3.8 T is present over its entire volume. A cross-sectional view of the CMS tracker has been presented in Fig. 2.10. The tracker is made up of a central barrel and endcap parts consisting of pixel and

strip layers. Both pixel and strip layers are made up of silicon sensors of different dimensions. The CMS tracker is the world's largest silicon tracker with over  $200\text{ m}^2$  of active silicon area. Whenever a charged particle passes through a silicon sensor, it results into generation of electron-hole pairs, which are measured in an outer circuit as a hit. Subsequent information of the large number of hits from different sensors leads to the reconstruction of the particle's track. Since the energy required to generate an electron-hole pair is small, the energy/momentum resolution of these sensors is very large. Also, since the electrons travel very fast to the outer circuit, the time resolution is better. The charged particles of different momentum curved differently under the effect of the magnetic field and the tracker records the particle's tracks and momentum by finding their positions and curvature at various key points.

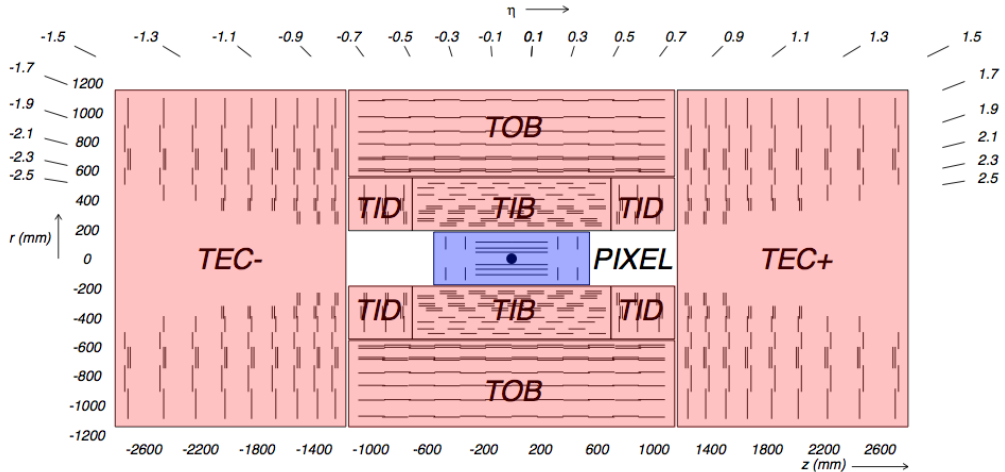


Figure 2.10: A cross-sectional view of the CMS tracker system in  $r$ - $z$  plane, with each line representing a silicon detector module.

The tracker has to face around 1000 particles coming from each bunch crossing at every 25 ns which lead to high radiation doses in the detector. So it should be able to operate in such a harsh environment in addition to dealing with high occupancy rate as well as providing high granularity and quick response [111]. The silicon detector technology meets all these goals very efficiently. The number of tracker layers is a tradeoff among the tracking efficiency and material budget [112]. On one side, more layers leads to more hits and precise track reconstruction. While on other side, large amount of material inside the tracker leads to multiple scattering which in turn can spoil proper tracking too.

In order to reconstruct a track using hits, the simplest approach is to start

from a hit in the innermost layer and in radial direction, project a cone on the next layer. If the next layer contains no hit within the cone, leave the starting point considering it a noise or a particle of very low energy. Otherwise, keep on repeating the procedure until last layer is reached. A more advanced approach start the search from the outermost layer along with taking additional information from other sub-detectors. A description of pixel and strip layers of CMS tracker has been provided below.

#### 2.2.1.1.1 Pixel detector

The high precision pixel detector [113] is the innermost detector of the CMS tracker. Since the particle flux near the collision point is very large, a small-scale pixel geometry is constructed to achieve unambiguous track reconstruction and precise vertex determination. The particles with relatively long lifetime, such as b and c quarks, arise from primary vertex but decay after travelling small distances, forming secondary vertices. The pixel detector is designed to distinguish these secondary vertices from the primary collision point.

The pixel detector consists of three concentric barrel layers and two endcap disks on both sides (shown in Fig. 2.11), covering a pseudorapidity region of  $|\eta| < 2.5$ . The barrel layers are 53 cm long and are present at the radii of 4.4, 7.3 and 10.2 cm from the beam line. The two endcap disks are extended in radius from 6 cm to 15 cm and are present at  $\pm 34.5$  and  $\pm 46.5$  cm from the collision point. The detector is equipped with a total of about 66 million pixels, each having a size of  $100 \times 150 \mu\text{m}^2$ . The occupancy rate of each pixel is of the order of 0.1% per LHC bunch crossing.

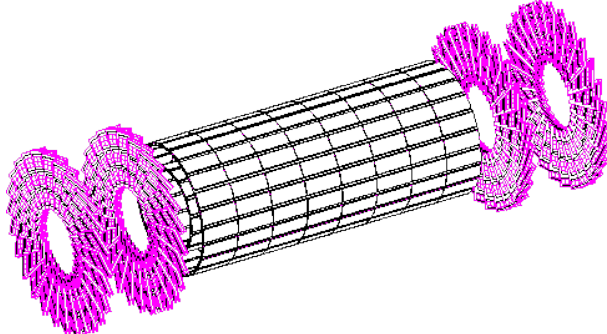


Figure 2.11: A schematic layout of the CMS pixel detector.

The pixel detector has performed exceedingly well during Run I, providing a

resolution of around  $10\mu\text{m}$  in  $r - \phi$  and  $20\text{-}40\mu\text{m}$  in  $z$  direction along with an overall efficiency of more than 99%. The LHC Run II started in 2015 with an increased center of mass energy of 13 TeV and a lower bunch crossing frequency of 25 ns. During overall Run II phase, a peak instantaneous luminosity of  $2 \times 10^{-34} \text{ cm}^{-2}\text{s}^{-1}$  was achieved. It also saw a pileup rate of more than 50. Under these conditions, the current pixel detector will suffer from increased fake rates and reduced resolution due to higher occupancy. So in order to maintain the performance of pixel detector, an upgrade known as “Phase1 Pixel Upgrade” [114, 115] was performed during the technical stop at the end of 2016. The upgraded pixel detector features 4 barrel layers and a turbine-like module arrangement for endcap disks (as shown in Fig. 2.12). Light-weight support structures and 2-phase  $\text{CO}_2$  cooling has been introduced to keep the optimum material budget. A comparison of the two detector configurations using tracking efficiency and fake rate as a function of pileup are presented in Fig. 2.13.

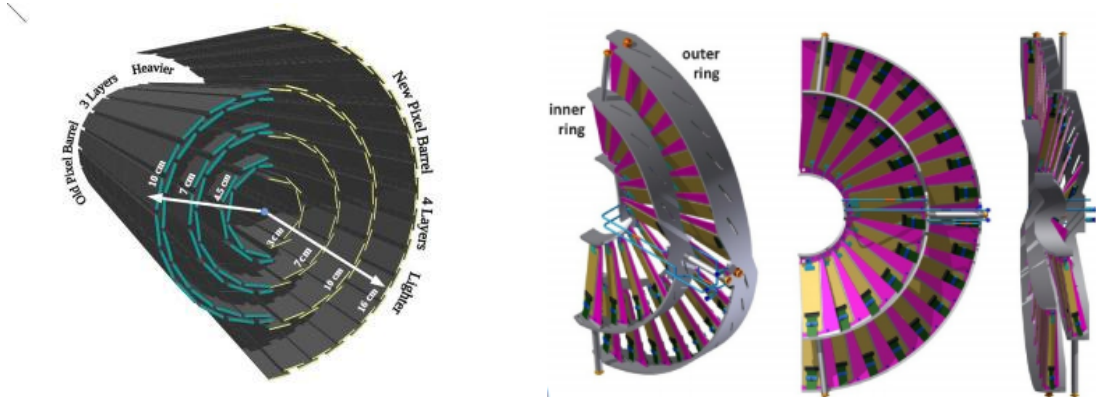


Figure 2.12: A schematic representation of the upgrades in pixel detector barrel (left) and endcaps (right) during Phase1 Pixel Upgrade.

### 2.2.1.1.2 Silicon strip detector

The silicon strip tracker [109, 110] is present outside the pixel detector and consists of more than 15000 single or double sided (shown in Fig. 2.10 by single and double lines) modules. Since the particle flux reduces in strip tracker, the dimensions of strip modules are kept larger than that of pixel detector modules. The size of modules also increases with distance to keep the occupancy level at around 1%. The modules are of rectangular shape in barrel region while that of trapezoidal shape in the endcap region. The strip tracker consists of four subsystems: The Tracker Inner Barrels (TIB), Tracker Inner Disks (TID), Tracker Outer Barrels (TOB) and Tracker EndCaps (TEC).

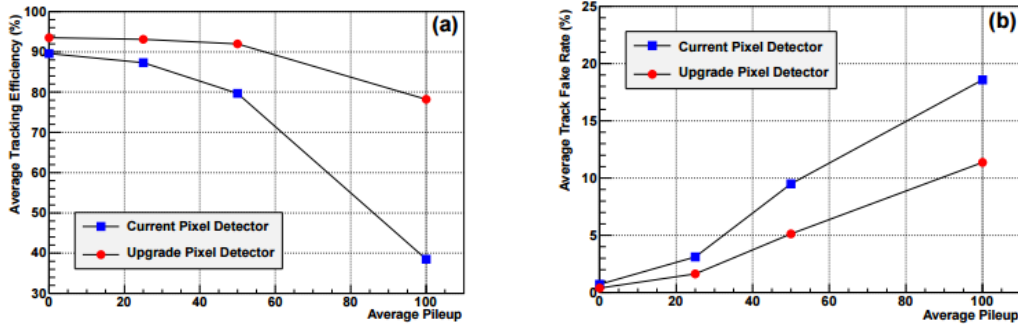


Figure 2.13: Performance measurement of the older pixel detector (blue) and the upgrade pixel detector (red) using  $t\bar{t}$  events, showing tracking efficiency (left) and fake rate (right) as a function of per event pileup [115].

The TIB and TID are extended up to a radius of 55 cm and consists of 4 barrel + 3 endcap layers. The modules in TIB/TID are  $320\mu\text{m}$  thick and delivers up to 4 measurements in  $r - \phi$  direction, providing a position resolution of  $23\mu\text{m}$  in the inner two layers and  $35\mu\text{m}$  in the outer two layers. The outer barrel layer TOB is made up of 6 layers of  $500\mu\text{m}$  thick sensors extended up to an outer radius of 116 cm which provides 6 more measurements in  $r - \phi$  direction, corresponding to a resolution of  $53\mu\text{m}$  in the initial four layers and  $35\mu\text{m}$  in the last two layers. The TOB covers a  $z$  range up to  $\pm 118$  cm. Outside this range,  $\pm$ TEC occupies the region from 124 – 282 cm in  $\pm z$  and 22.5 – 113.5 cm in  $\pm r$ . Each of the TEC is made up of 9 disks, thereby providing 9 measurements in  $r - \phi$  per trajectory.

The transverse momentum resolution of the tracker varies in the range from 0.7% at 1 GeV to 1.5% at 100 GeV.

### 2.2.1.2 Calorimeter

A calorimeter is a device that is used to measure energies of different type of particles. The incident particle interacts with the material of the calorimeter and produces a cascade (shower) of secondary particles of progressively lower energies, until the energies fall below a critical value which is then dissipated in ionization or excitation of the atoms of the material. The subsequent energy released by the atoms is captured by the photo-detector which through photoelectric effect, yield an electronic signal that provides a measurement of the particle's energy. In case of the sampling calorimeters, the medium that activate the particle shower is known as the passive medium (absorber) while the one that absorb the shower

particles and lead to the energy measurement, is known as the active medium (scintillator). Calorimeters has the capability to stop almost all particles except muons and neutrinos.

Calorimeters are broadly divided into two categories: Hadronic and Electromagnetic, depending on the particle type. They can also be classified on the basis of their composition into sampling and homogeneous calorimeters. A sampling calorimeter is the one that consists of alternate layers of two materials acting as passive and active mediums while a homogeneous calorimeter is build up of only one type of material that accomplish both the tasks. An advantage of sampling configuration is that both the materials used are well-suited for their tasks. A very high density material is used as passive medium which results into the quick evolution of the shower into a limited space, so sampling calorimeters can be made compact as compared to homogeneous calorimeters. However, it has a disadvantage that part of the shower energy get deposited in the passive medium and left unmeasured.

The CMS consists of Electromagnetic calorimeter (ECAL) just outside the tracker, followed by Hadronic calorimeter (HCAL), both contained inside the solenoidal magnet. A short description of each one is considered below.

#### 2.2.1.2.1 Electromagnetic calorimeter

The CMS ECAL measures the energy of electromagnetically interacting particles, primarily photons and electrons. The photons interact with the material of the detector mainly through pair production for energies above 1 MeV and through Compton scattering and photoelectric effect for energies below 1 MeV. On the other hand, electrons mainly interact via bremsstrahlung for energies above 10 MeV and through ionization and excitation for energies below it. As a consequence, high energy electrons and photons, inside ECAL, produce a number of secondary particles, thereby generating electromagnetic (EM) showers. The EM showers are characterized by a material dependent parameter, the radiation length denoted as  $X_0$ , which is the average distance  $x$  travelled by an electron before losing an energy equivalent to  $1/e$  times its original energy i.e.  $E = E_0 e^{-\frac{x}{X_0}}$ . It is also equivalent to  $7/9$  times the free path travelled by photon before converting into an  $e^+e^-$  pair.

As a result of particle multiplication and faster interaction, the amount of material required to contain an EM shower is rather small. Therefore, the

ECAL [109, 116] (shown in Fig. 2.14) is constructed as a homogeneous calorimeter made up of lead tungstate ( $\text{PbWO}_4$ ) scintillating crystals. It is a highly dense material ( $8.28 \text{ g/cm}^3$ ) with a radiation length of  $0.89 \text{ cm}$  and Molière radius of  $2.2 \text{ cm}$ , allowing a design of fast, granular and radiation resistant calorimeter. The crystals are designed to provide very good energy resolution of electrons and photons required for CMS physics program. These are arranged in carbon fibre matrices to provide optical isolation.

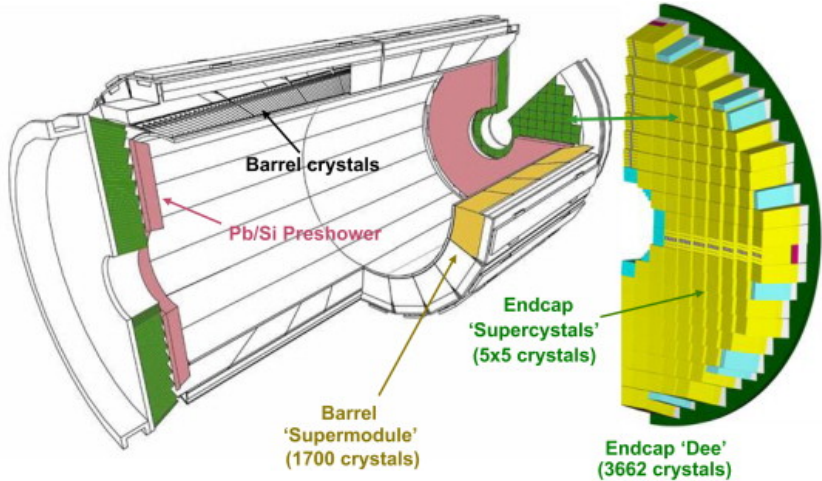


Figure 2.14: A layout of the CMS Electromagnetic calorimeter displaying the arrangement of crystals in barrel and endcaps with the preshower present in front.

The ECAL barrel (EB) is extended upto  $|\eta| < 1.479$  and consists of 61,200 crystals providing 360-fold granularity in  $\phi$  and  $(2 \times 85)$ -fold granularity in  $\eta$  direction. The crystals are of trapezoidal shape having a front cross section of  $22 \times 22 \text{ mm}^2$ , a rear cross section of  $26 \times 26 \text{ mm}^2$  and a length of  $230 \text{ mm}$ , equivalent to  $25.8X_0$  implying that it is able to contain  $99.999\ldots\%$  of  $e/\gamma$  energy. These crystals are assembled into 36 supermodules, each weighing around 3 tonnes and containing 1700 crystals. Each supermodule covers  $20^\circ$  in  $\phi$  and half barrel in  $\eta$ . The avalanche photodiodes (APDs) are used as photo-detectors to capture the scintillating light generated in the crystals upon interaction. These are made up of semiconducting silicon and have an active area of  $5 \times 5 \text{ mm}^2$ . The relatively low light yield of  $\text{PbWO}_4$  crystals is compensated by the signal amplification by APDs through avalanche process. In addition, insensitivity of APDs towards high magnetic field and high radiation environment, makes them convenient for EB.

The flat circular ECAL endcaps (EE) cover the barrel at both the ends in the pseudorapidity range  $1.479 < |\eta| < 3.0$ , each consisting of 7,324 crystals arranged

in  $5 \times 5$  crystal units, known as supercrystals. The trapezoidal crystals have a front face of  $28.62 \times 28.62 \text{ mm}^2$ , a rear face of  $30 \times 30 \text{ mm}^2$  and a length of  $220 \text{ mm}$  ( $24.7X_0$ ). Endcaps use vacuum phototriodes (VPTs) as photo-detectors since these can work in high radiation environment compared to APDs. Each VPT has a diameter of  $25 \text{ mm}$  and an active area of  $280 \text{ mm}^2$ . In front of each ECAL endcap is present a high granularity sampling calorimeter, known as ECAL Preshower (ES), made up of alternating layers of lead (passive medium) and silicon strips (active medium). It covers a pseudorapidity range of  $1.653 < |\eta| < 2.6$  and forms a disc of  $2.5 \text{ m}$  circumference. The disc is about  $20 \text{ cm}$  thick and has a  $50 \text{ cm}$  diameter hole in the middle for the passage of beam pipe. The principle aim of ES is to identify and stop overlapping photons coming from the decay of  $\pi^0$  so as to prevent false signals. The high density of lead stimulate quick showering, thereby resulting into the shower containment in a very small volume. Around  $95\%$  of incident photons start showering in the first lead plane.

Many contributions deteriorate the actual energy resolution of any realistic calorimeter. The energy resolution of ECAL (for energies below  $500 \text{ GeV}$ ) can be written in general as:

$$\frac{\sigma}{E} = \frac{S}{\sqrt{E}} \oplus \frac{N}{E} \oplus C \quad (2.5)$$

where  $\oplus$  corresponds to quadratic sum which implies that the contributions of different terms are independent from each other. The first term  $S$  is known as stochastic or sampling term. It considers the statistical fluctuations due to the shower fluctuations, lateral shower leakage, photo-detector inefficiencies, efficiency loss due to the shower containment in the passive medium of preshower etc. The second term  $N$  corresponds to the noise term arising due to instrumental effects, light-attenuation, pileup effects etc. The last term  $C$  is a constant term and it includes effects from imperfections in calorimeter construction, inter-calibration errors, longitudinal shower leakage, fluctuation in energy deposition in the dead areas of calorimeter etc.

The test beam studies [117] were performed using a block of  $3 \times 3$  crystals and various terms involved in energy resolution were computed. These terms for barrel region are:  $S = 2.8\%$ ,  $N = 124 \text{ MeV}$  and  $C = 0.3\%$  while for endcap region are:  $S = 5\%$ ,  $N = 500 \text{ MeV}$  and  $C = 0.3\%$ .

### 2.2.1.2.2 Hadronic calorimeter

The CMS HCAL has been designed to measure energy of particles (hadrons) interacting via strong force. Hadrons interact with the material of the detector through strong nuclear interactions, resulting into the production of a large number of secondary hadrons, thereby activating a hadronic shower. A majority of these shower particles, around 90%, are pions. Among these, the neutral pions ( $\pi^0$ ) decay electromagnetically into two photons, thereby generating a component of EM shower within a hadronic shower. The fraction of energy of a hadron taken off by the EM component is denoted as  $f_{\text{EM}}$  and it varies from event-to-event. This fraction depends on the energy of initial hadron and varies from 30% for a 10 GeV hadron to 50% for a 100 GeV hadron. Also, a significant fraction of shower particles lose their energy as nuclear binding energy in nuclear reactions. This energy does not appear as a signal in the calorimeter and therefore, dissipate as invisible energy. As a consequence, the calorimeter signal for a hadron is usually smaller than an electron having same energy, a phenomenon known as non-compensation, also denoted as  $e/h$  ratio. These two features of hadron showers result into a non-linearity in the energy measurement of hadrons by HCAL.

The shower profiles of hadrons are characterized by nuclear interaction length,  $\lambda_{\text{int}}$  (expressed in g/cm<sup>2</sup>) which is the mean distance traversed by a hadron before undergoing a nuclear interaction. Usually, the interaction length of a hadron is much larger than the radiation length of an electron of same energy, e.g. in copper,  $X_0 = 1.4 \text{ cm}$  while  $\lambda_{\text{int}} = 15 \text{ cm}$ . This implies that a large amount of material is required to contain a hadron of a particular energy compared to an electron of same energy, not possible to achieve with homogeneous calorimeter. Therefore, the hadron calorimeter always use sampling configuration. A properly designed sampling detector achieves compensation of hadronic signals by the use of various techniques and sampling fractions [118].

The HCAL [119] is a sampling calorimeter constructed of a dense absorber material made up of brass/steel plates interleaved with plastic scintillator tiles, which are read out via embedded wavelength-shifting (WLS) fibres. This configuration is chosen for both barrel and endcap regions of HCAL due to the non-magnetic behaviour, high absorption length and good mechanical strength of brass while long term stability and radiation hardness of plastic scintillators. The detector is assembled in such a way that it does not have any cracks or dead areas in

$\phi$ . The scintillator tiles emit blue-violet light upon particle interaction, which is then converted into green light by WLS fibres. These optical signals are then converted into electronic signals by the use of Hybrid Photodiodes (HPDs). The HCAL constitutes of four sections: HCAL Barrel (HB) [120], HCAL Endcaps (HE) [121], HCAL Forward (HF) [122], and HCAL Outer (HO) [123]. The HCAL, in association with ECAL, provides the energy/direction measurements of hadrons. A schematic view of a section of HCAL is presented in Fig. 2.15.

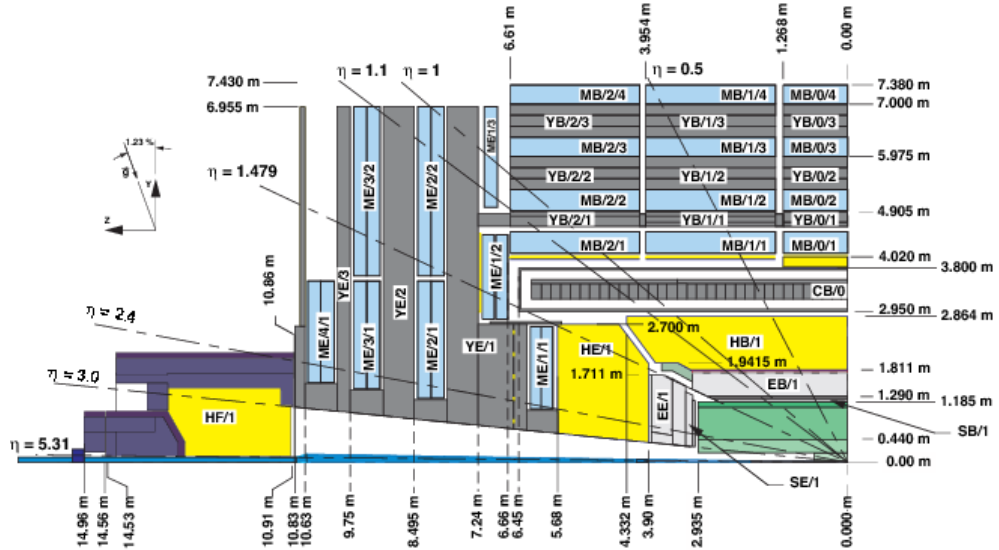


Figure 2.15: A schematic view of a quadrant of the CMS Hadron calorimeter presenting different sub-detectors (in yellow color).

The HCAL barrel covers a pseudorapidity range of  $|\eta| < 1.3$  and is made up of two half barrels, each made of 18 azimuthal wedges, each covering  $20^\circ$  in  $\phi$ . Each wedge is sliced into 16 absorber plates, with front and back plates made of steel and rest made of brass (a Cu-Zn alloy). The plastic scintillating tiles with WLS fibres are arranged into trays containing many tiles and are inserted between each plate to construct a sampling configuration. Each wedge is further partitioned into  $4\phi$  sectors while the plastic scintillators are further partitioned into  $16\eta$  sectors, resulting into a segmentation of  $\Delta\phi \times \Delta\eta = 0.087 \times 0.087$ . The HB is situated between EB (at  $r = 1.77$  m) and superconducting magnet (at  $r = 2.95$  m), resulting into highly constrained material amount. The total thickness of HB corresponds to  $5.82\lambda_{\text{int}}$  at  $\eta = 0$  and  $10.6\lambda_{\text{int}}$  at  $\eta = 1.3$ , ECAL also adds a thickness of  $1.1\lambda_{\text{int}}$  to HB material. In order to ensure the proper energy containment of hadronic showers, a complementary detector layer of same configuration known as HO, is positioned outside the magnet coil which acts as a tail-catcher for any late starting

showers. It provides an additional thickness of  $1\text{--}2\lambda_{\text{int}}$  to HB showers. The high pseudorapidity region,  $1.3 < |\eta| < 3.0$  has been instrumented using HE on both sides of HB. The endcaps are made of 17 brass plate layers with plastic scintillator tiles accommodated in between. Including with EE, it corresponds to a total thickness of around  $10\lambda_{\text{int}}$ .

The high radiation environment ( $3.0 < |\eta| < 5.0$ ) near the beam pipe is armed with a more robust hadron forward (HF) calorimeter made up of quartz fibres as active medium and steel as the absorber medium. The front face of HF is located at a distance of 11.2 m from the interaction point. The structure is divided into 36 azimuthal wedges of steel, 18 wedges on each side of collision point and composed of 5 mm thick scintillator plates along with WLS fibres. A signal in the form of Cherenkov radiation is produced in HF when a charged particle from the shower enters the active medium (quartz) with a velocity greater than that of light in the medium. The HF has been utilized to improve the  $E_{\text{T}}^{\text{miss}}$  measurements and identify/reconstruct very forward jets which can contain distinguishing features of many physics processes. The HF is also used in the measurement of online luminosity of CMS.

The energy resolution of CMS HCAL is parametrized as:  $\frac{\sigma}{E} = \frac{A}{\sqrt{E}} \oplus B$ , with the parameters,  $A = 0.847 \text{ GeV}$  and  $B = 0.074$  for HB and HE and  $A = 1.98 \text{ GeV}$  and  $B = 0.09$  for HF.

### 2.2.1.3 Solenoidal magnet

The CMS uses a large solenoid magnet [124] as its central device around which the detector has been constructed. In order to achieve precise measurements and resolutions of energy/momenta of charged particles coming from the collisions, CMS has deployed a large magnetic field of 3.8 T. A charged particle in a uniform magnetic field  $\vec{B}$  experience a force equal to  $F = qvB \sin \theta$ , where  $q$  is the particle's charge,  $\vec{v}$  is the particle's velocity and  $\theta$  is the angle between  $\vec{v}$  and  $\vec{B}$ . In this magnetic field, the particle will traverse a curve of radius  $\frac{mv}{qB \sin \theta}$ ,  $m$  being the mass of particle, which implies that the particles of different initial velocities or momenta will be curved differently inside field  $\vec{B}$ . Therefore, measurement of the angle and radius of curvature of charged particles inside  $\vec{B}$  can be used to get an estimate of particle's momentum. Also, the momentum resolution depends on the magnitude of magnetic field  $\vec{B}$  and length of solenoid  $L$  as  $\frac{\Delta p}{p} = \frac{p}{BL^2}$ , stating that a large

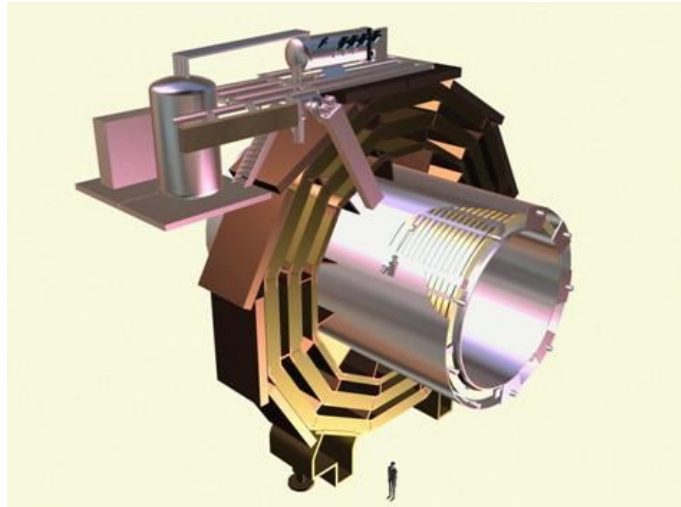


Figure 2.16: A schematic view of the solenoidal magnet used in the CMS detector, showing the coil and the central return yoke.

resolution (less  $\Delta p$ ) can be achieved by the use of a high magnetic field of large size.

The CMS magnet as shown in Fig. 2.16 is a solenoidal magnet made of superconducting Nb-Ti coils which produce an intense magnetic field of 3.8 T when a current of 19,500 Ampere is passed through them. The magnet with a length of 13 m and an internal diameter of 5.9 m fit snugly the tracker and calorimeters inside. It consists mainly of three parts: the coil, vacuum tank and yoke. The vacuum tank acts as a cryostat and provide the essential cooling to solenoid using liquid He. The return yoke is made up of iron and is present outside the magnet coil reaching an outer diameter of 14 m. It is responsible for return of magnetic flux with a field of 2 T. The yoke is a 12-sided structure made up of 11 discs, 5 in barrel and 6 in endcaps, the muon chambers are interleaved in this. The total energy stored inside the magnet amounts to around 2.6 GJ.

#### 2.2.1.4 Muon detector

The CMS has been specifically designed for precise identification, momentum resolution and triggering of muons within a range  $|\eta| < 2.4$  and  $p_T \leq 1 \text{ TeV}$ . Muons, though interact electromagnetically, do not lose much of their energy via bremsstrahlung owing to their high mass as compared to electrons. They interact primarily through ionization loosing an energy on the average of  $1\text{-}2 \text{ MeV/g/cm}^2$ . Due to their less interacting nature, they penetrate the material of ECAL and HCAL, so the muon chambers for their detection are installed at the very edge of

the detector.

The CMS muon [125] system has been divided into four stations interleaved with the return yoke and having a magnetic field of 2 T. The barrel muon detector is also longitudinally divided into five wheels labelled as YB0, YB $\pm$ 1, YB $\pm$ 2, with each wheel being further divided in the azimuth direction into 12 sectors of  $30^\circ$  each. It uses three different kind of detectors to observe muons: Drift Tubes (DTs), present in the barrel region upto  $|\eta| < 1.2$ ; Cathode Strip Chambers (CSCs), present in the endcap region for  $0.9 < |\eta| < 2.4$ ; and Resistive Plate Chambers (RPCs), present in barrel as well as endcaps. Whenever a particle passes through these chambers, it leaves its signature in the form of hits. Tracking the particle's position in multiple layers and combining the information from tracker, leads to a precise determination of the position and momentum of the particle. The DTs/CSCs are good in position measurements while the RPCs provide fast response, so a combination of the three result into a robust muon detector. Diagrams representing the mechanical layout of CMS muon detector and the trajectory of muon through muon stations is shown in Fig. 2.17.

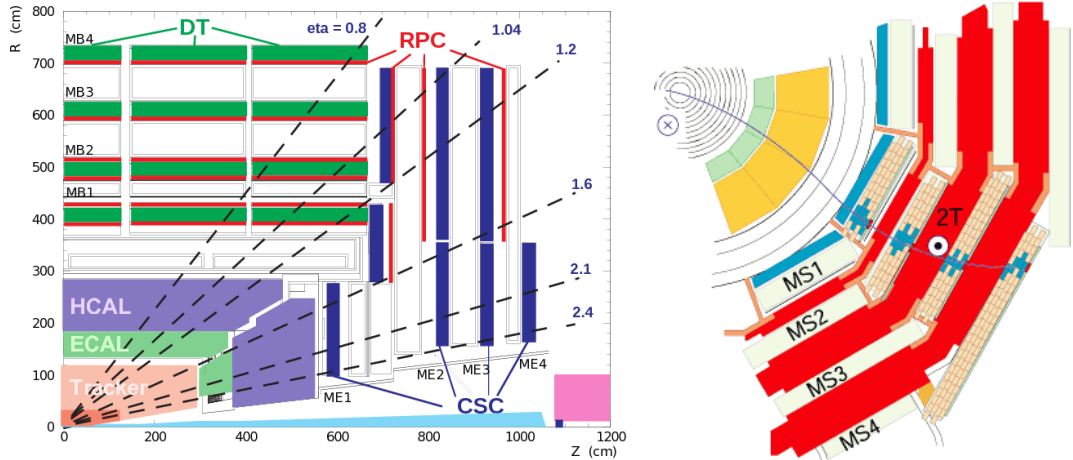


Figure 2.17: A schematic view of the solenoidal magnet used in CMS, showing the coil and the central return yoke. The trajectory of a muon through the muon stations is also presented.

The drift tubes are organized into 4 stations labelled as MB1, MB2, MB3 and MB4, which forms concentric cylinders around the beam pipe. Each of the inner three stations are composed of 12 drift chambers, with each chamber containing many drift tubes. These chambers are further grouped into three superlayers denoted as SL1, SL2 and SL3, each consisting of four chambers. SL1 and SL2 provides the co-ordinates of incident muons in  $r - \phi$  plane while SL2 measures the

co-ordinates in  $r - z$  plane. The outermost station consists of two superlayers only. The choice of drift chambers is made in barrel due to the low particle rate and uniform magnetic field. Each drift tube contains a anode wire of  $50\mu m$  diameter and two electrode plates to create electric field. The tube walls are grounded and act as cathodes. The drift tube is filled with a gas containing a mixture of Ar (85%) and CO<sub>2</sub> (15%). The voltage difference between wire and walls is about 1.8 kV. When a muon pass through the gas volume, it knocks off electrons which travel to the anode wire, carrying along the information of incident particle. The DTs provide a signal gain of  $10^5$  and a drift time of 380 ns.

The CSCs have been deployed in the high radiation and uneven magnetic field environment in the endcaps. Owing to their quick response time, high granularity and radiation hardness, the CSCs are well qualified to identify muons in the range  $0.9 < |\eta| < 2.4$ , overlapping with DTs in  $0.9 < |\eta| < 1.2$ . The CSC chambers are of trapezoidal shape placed perpendicular to the beam line and cover  $10^\circ$ - $20^\circ$  in  $\phi$ . These are organized in 4 stations per endcap, labelled as ME $\pm 1$ , ME $\pm 2$ , ME $\pm 3$  and ME $\pm 4$ , each station containing a number of CSCs. Each CSC consists of an array of positive anode wires made of tungsten held perpendicular to the negative cathode strips made of copper, in a gas mixture of Ar (40%), CO<sub>2</sub> (50%) and CF<sub>4</sub> (10%). When a muon enters a CSC, it knocks off electrons from the gas atoms, which then flock towards the anode wires resulting into an electron avalanche. The positive gas ions move towards cathode strips and induce a charge pulse. Since the anode wires and cathode strips are present in perpendicular direction, these provide two position co-ordinates corresponding to each particle. This arrangement in CSCs also results into fast response making them convenient for triggering. Each CSC is composed of six anode wires interleaved with seven cathode strips, providing the measurements in  $r - \phi$  plane.

The RPCs are parallel plate gaseous detectors with fast response time and adequate position resolution making them suitable for muon triggering. The RPCs are installed both in barrel (480 chambers) and endcaps (432 chambers) with two chambers of rectangular shape per DT chamber in barrel and one chamber of trapezoidal shape per CSC chamber in endcaps. The RPCs have the ability to tag a particle in a time frame much lesser than the bunch crossing time, making them ideal for triggering. The RPC is composed of two gaps, each operating in avalanche mode and read-out strips are inserted in-between. The total signal induced by the

RPC is sum of signal induced in each gap. However, in order to ensure proper stability and operation of the RPC, an intensive control of humidity, temperature and pressure is required.

The muon system of CMS is made up of around  $25000\text{ m}^2$  area and more than a million readout channels. Considering only the muon system without any information from tracker (stand-alone muon), a momentum resolution of around 9% is obtained for a muon of  $p_T \leq 200\text{ GeV}$  in low  $\eta$  region. For a high  $p_T$  muon ( $\sim 1\text{ TeV}$ ), the resolution varies from 15-40% for different  $\eta$ . Adding tracker information (global muon) results into an improvement in momentum resolution of around 1% for low  $p_T$  muons and around 5% for high  $p_T$  muons.

#### 2.2.1.5 CMS upgrade during Long Shutdown 1

During LS1 in 2013-2015, minor repair and maintenance work were performed on most of the CMS sub-systems, except for some major improvements that include: Installation of new pixel tracker layer (explained in Section 2.2.1.1) which was actually done after LS1 and during the technical stop at the end of 2016, installation of new photo-detectors to improve signal-to-noise ratio in HCAL outer barrel, installation of the fourth RPC disk in the endcap region of the muon detector which was actually the part of the first CMS technical design report and installation of around 72 new chambers in CSC along with 468 old chambers. The electronics have also been updated to handle high collision rates.

### 2.2.2 CMS Trigger and Data Acquisition System

Most of the LHC collision data consists of “soft” particles which do not participate in any interesting process. Also, at each bunch crossing, the collisions amount to a raw data of approximately 1 MB, which at the crossing rate of 40 MHz (25 ns), results into around 40 TB data per second. It is almost impossible to store and process such a large amount of data. Therefore, to reduce the data rate while keeping the potentially interesting events for further analysis, a hardware and software based automated system, referred to as the CMS trigger system [126] has been designed together with a Data AcQuisition (DAQ) system [127], as shown in figure Fig. 2.18. The trigger system consists of two layers: a hardware based trigger known as Level-1 (L1) trigger and a software based trigger known as the High Level Trigger (HLT), reducing the event rate to an average of a few 100 Hz

to a maximum of 1 kHz. The data passing through both the trigger levels is stored for offline physics analysis. In order to obtain the required data rate, sometimes the triggers are prescaled at L1 or at HLT level, thereby storing only a fraction of selected events. DAQ acts as a bridge between the two trigger layers, it gathers data from first trigger layer, digitizes and build it and pass it to second trigger layer.

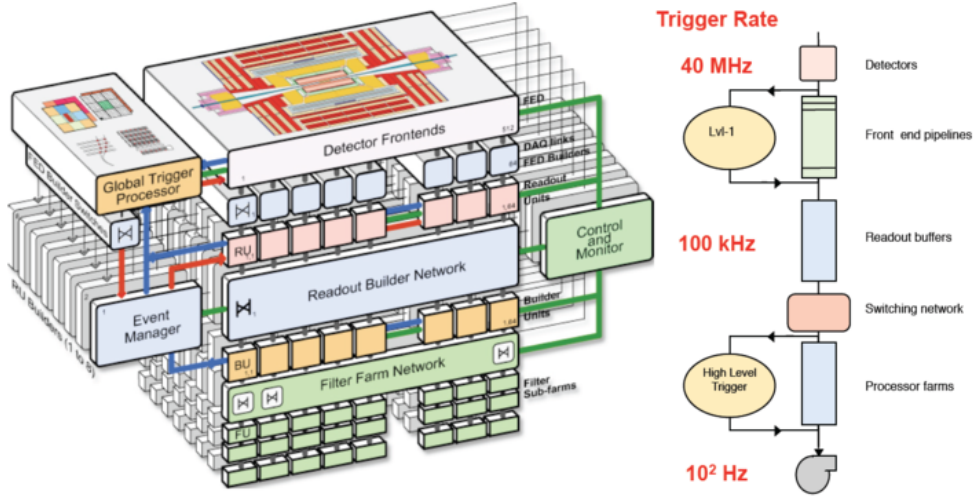


Figure 2.18: CMS Data Acquisition and trigger system.

### 2.2.2.1 Level-1 trigger

The Level-1 trigger of CMS is a set of hardware based triggers that rely on custom electronics. It has been designed to produce an output data rate limit of 100 kHz. The L1 triggers are implemented as custom hardware processors and considers only low resolution, coarsely segmented data from ECAL, HCAL and muon systems while keeping the high resolution data in the pipelined memories present in the front-end electronics. The L1 stores data in pipeline for  $3.2\mu s$  during which it transmits its decision to detector electronics. The L1 trigger consists of a number of hardware components including field-programmable gate-array (FPGA) technology, ASICs and programmable lookup tables (LUTs). A block diagram representing the architecture of L1 trigger system is shown in Fig. 2.19.

The L1 trigger consists of local, regional and global components. At the top are the local triggers, also known as Trigger Primitive Generators (TPGs), which takes the information from the energy deposits in calorimeter towers and hit patterns in muon chambers. The information from TPGs are then passed on to

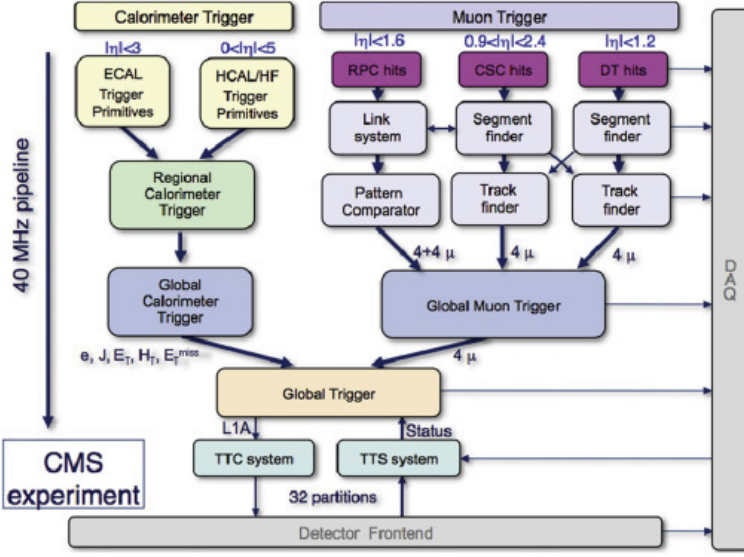


Figure 2.19: An architecture of CMS Level-1 trigger system.

the regional triggers. The regional calorimeter triggers (RCTs) makes use of this information and forms sorted and ranked trigger objects like electrons, photons and jets. The regional muon triggers (RMTs) join the segments and complete the tracks along with assigning physical parameters to them. The regional triggers passes these objects along with various information to the Global Calorimeter Triggers (GCTs) and Global Muon Triggers (GMTs) which sort out the highest ranked calorimeter and muon candidates along with determining various physics parameters like  $E_T$ ,  $E_T^{\text{miss}}$ , number of jets,  $H_T$  etc. This information from GCTs and GMTs are then passed on to the Global triggers (GTs), the top level entity of L1 hierarchy, which makes the final decision of keeping or rejecting the event by applying the programmable topological cuts and energy thresholds on the objects and issues the final Level-1 Accept (L1A) decision. The L1A is then passed on to the Trigger Timing and Control (TTC) system for transferring it further to the detector front-end, from where it goes into the DAQ system. The TTC also interfaces with the LHC machine to provide clock and orbit information. The GT sends a command by the use of TTC in order to keep all the detectors and their electronics well in synchronization.

### 2.2.2.2 High level trigger

The CMS high level trigger accepts the output of L1 trigger and process it further by using a software (written mostly in C++) based trigger system implemented in a filter farm consisting of more than thousand commercial processors. All major

aspects of offline reconstruction code are included in the filter farm software and is designed to reduce data rate to a minimum of few 100 Hz. The average time taken in HLT processing is around 100 ms. It employs the use of high resolution data and utilize many sophisticated algorithms to identify interesting events for further storage. The HLT is based on highly flexible programming environment such that the changes in the algorithms can be easily done to improve the various selections and to deal with unexpected experimental conditions. A set of algorithms that reconstruct the physics candidates (known as producers) and apply various selections to the reconstructed objects (known as filters) is known as a “trigger path”; a number of trigger paths together constitute a “HLT trigger menu”. Within a trigger path, the various algorithms are arranged in an increasing order of complexity, with the most complex algorithms like the b-tagging, are executed in the end. Events that pass any of the trigger paths within a trigger menu are considered for further analysis and are sent to storage manager where these are stored on disks and are sent to CMS Tier-0 system present at CERN for offline processing and permanent storage.

#### 2.2.2.3 Data acquisition system

The CMS DAQ mainly work as a carrier that gathers the data stored in detector’s front-end modules at the Level-1 accept rate and deliver it to HLT filter farms for further processing. It operates at an input data rate of 100 kHz, the output rate of L1 trigger. The complete processing of DAQ is summarized as follows: First of all, the front end systems (FESs) store data continuously in 40 MHz pipelined buffers. As the synchronous L1 trigger comes, data are extracted from FES via TTC and pushed into front end drivers (FEDs). The FEDs digitize, convert and zero suppress the data and then transfer it to front end read out links (FRLs) that merge data from different FEDs. These FRLs are known as event builders as these built a complete event by assembling the event fragments from all FEDs belonging to same L1. The data from FRLs are then transmitted into filter units (FUs). The HLT is mounted over FUs and use its computing power to perform its operations. These FESs, FEDs, FRLs, FUs all forms the different parts of DAQ system. A Trigger-Throttling System (TTS) has also been designed to protect DAQ against any back-pressures.

### 2.2.3 CMS data management

The raw data after passing the various triggering stages, is managed further by the use of the LHC computing grid [128]. The grid is constituted of four levels/tiers, referred to as Tier-0 (T0), Tier-1 (T1), Tier-2 (T2) and Tier-3 (T3). Each tier consists of a number of computer facilities and provides a set of dedicated services. The Tier-0 is the data center present at CERN, it contributes less than 20% of total grid computing capacity but it is responsible for maintaining a full copy of raw data, for performing calibration and prompt reconstruction (prompt-reco) and for distributing the raw and prompt-reco data to Tier-1 centers. Tier-1 is a group of around 13 computer centers located in various part of the world and joined together via optical-fibre links operating at a speed of 10 gigabytes/sec. The T1 centers together maintain a second copy of raw data, produce various Monte Carlo (MC) samples<sup>3</sup> and re-reconstruct the raw data along with distributing it to various Tier-2 centers. The T2 centers are the sites where physicists can log-in and perform their analysis within the CMSSW environment. These centers also produce the MC samples and share them with T1 centers for storage and distribution to other sites. There are around 155 T2 sites distributed all over the world. The Tier-3 consists of local computing resources at various universities and institutes which individual users can access from any place around the world using grid, and can use for storage and data analysis.

The data present at various tiers are managed by the use of three data management tools [129]: Physics Experiment Data Export (PhEDEx) [130, 131], Data Bookkeeping Service (DBS) [132] and Data Aggregation Service (DAS) [133]. The PhEDEx service provides data information access through the central PhEDEx database, perform operations such as requesting data transfer or data deletion and transport the data among the different CMS sites along with keeping a track. The DBS service keeps a metadata catalog of all the CMS data used by physicists as well as the various production and analysis systems. The DAS service provides the user an overview of all the available datasets and keep a mapping between the datasets and corresponding file blocks.

---

<sup>3</sup>simulated data samples, more information provided in Chapter 3

## 2.2.4 CMS software and computing

The CMS physics analyst perform various analyses using a collection of softwares based on C++ and python, referred to as the “CMS Software frameWork” (CMSSW) [104], installed at various T2 and T3 centers. A number of services including simulations, calibration corrections or reconstruction etc. are supported by this framework. It consists of one main executable, known as cmsRun, along with many other plug-in modules, containing all the required codes for event processing. The cmsRun operates over a python configuration file that contains all the important information regarding the data and modules. The CMSSW software has been built over the concept of an “Event”. An Event contains the information of a particular collision in different data formats, a physics dataset consists of many events and are stored in the form of ROOT<sup>4</sup> [134] files. A RAW data format contains the output of online trigger decisions and has a size of 1.5 MB/event, the size of RAW data in a simulated sample is around 2 MB/event due to additional information. A RECO data format contains the offline reconstructed data that includes the high level physics objects such as electrons, photons, jets, b-jets, muons, taus  $E_T^{\text{miss}}$  etc., in convenient format and has a size of 250 kB/event. Usually, a RECO data format contains a large amount of unwanted information, so more compact data formats are obtained by filtering the RECO data. These data formats includes Analysis Object Data (AOD) and mini Analysis Object Data (mini-AOD), used in almost all physics analyses.

---

<sup>4</sup>ROOT is a data analysis framework



## BIBLIOGRAPHY

- [1] S. L. Glashow, “Partial Symmetries of Weak Interactions”, *Nucl. Phys.* **22** (1961) 579–588, doi:10.1016/0029-5582(61)90469-2.
- [2] A. Salam and J. C. Ward, “Electromagnetic and weak interactions”, *Phys. Lett.* **13** (1964) 168–171, doi:10.1016/0031-9163(64)90711-5.
- [3] S. Weinberg, “A Model of Leptons”, *Phys. Rev. Lett.* **19** (1967) 1264–1266, doi:10.1103/PhysRevLett.19.1264.
- [4] D. J. Gross and F. Wilczek, “Ultraviolet Behavior of Nonabelian Gauge Theories”, *Phys. Rev. Lett.* **30** (1973) 1343–1346, doi:10.1103/PhysRevLett.30.1343.
- [5] H. D. Politzer, “Reliable Perturbative Results for Strong Interactions?”, *Phys. Rev. Lett.* **30** (1973) 1346–1349, doi:10.1103/PhysRevLett.30.1346.
- [6] J. Dalton, “On the absorption of gases by water and other liquids”, *Memoirs of the Literary and Philosophical Society of Manchester* **1** (1805) 271–287, doi:10.1080/14786440608563325.
- [7] A. W. Thackray, “The Origin of Dalton’s Chemical Atomic Theory: Daltonian Doubts Resolved”, *Isis* **57** (1966) 35–55, doi:10.1086/350077.
- [8] J. J. Thomson, “Cathode Rays”, *Philosophical Magazine* **44** (1897) 293.
- [9] J. J. Thomson, “On the Structure of the Atom: an Investigation of the Stability and Periods of Oscillation of a number of Corpuscles arranged at equal intervals around the Circumference of a Circle, with Application of the Results to the Theory of Atomic Structure”, *Philosophical Magazine* **7** (1904) 237–265, doi:10.1080/14786440409463107.

- [10] E. Rutherford, “The scattering of alpha and beta particles by matter and the structure of the atom”, *Phil. Mag.* **21** (1911) 669–688, doi:10.1080/14786440508637080.
- [11] E. Rutherford, “The structure of the atom”, *Nature* **92** (1913) 423.
- [12] J. Chadwick, “Possible Existence of a Neutron”, *Nature* **129** (1932) 312.
- [13] A. Einstein, “On a heuristic viewpoint concerning the production and transformation of light”, *Annalen Phys.* **17** (1905) 132–148.
- [14] A. H. Compton, “A Quantum Theory of the Scattering of X-rays by Light Elements”, *Phys. Rev.* **21** (1923) 483–502, doi:10.1103/PhysRev.21.483.
- [15] A. Einstein, “On the electrodynamics of moving bodies”, *Annalen Phys.* **17** (1905) 891–921, doi:10.1002/andp.200590006.
- [16] P. A. M. Dirac, “The Quantum Theory of the Emission and Absorption of Radiation”, *Proc. R. Soc. Lond. A114* **243** (1927) 710.
- [17] C. D. Anderson, “The Positive Electron”, *Phys. Rev.* **43** (1933) 491–494, doi:10.1103/PhysRev.43.491.
- [18] R. P. Feynman, “Space-time approach to nonrelativistic quantum mechanics”, *Rev. Mod. Phys.* **20** (1948) 367–387, doi:10.1103/RevModPhys.20.367.
- [19] R. P. Feynman, “A Relativistic cutoff for classical electrodynamics”, *Phys. Rev.* **74** (1948) 939–946, doi:10.1103/PhysRev.74.939.
- [20] R. P. Feynman, “The Theory of positrons”, *Phys. Rev.* **76** (1949) 749–759, doi:10.1103/PhysRev.76.749.
- [21] J. S. Schwinger, “On Quantum electrodynamics and the magnetic moment of the electron”, *Phys. Rev.* **73** (1948) 416–417, doi:10.1103/PhysRev.73.416.
- [22] J. S. Schwinger, “Quantum electrodynamics. I A covariant formulation”, *Phys. Rev.* **74** (1948) 1439, doi:10.1103/PhysRev.74.1439.
- [23] S.-I. Tomonaga and J. R. Oppenheimer, “On Infinite Field Reactions in Quantum Field Theory”, *Phys. Rev.* **74** (1948) 224–225, doi:10.1103/PhysRev.74.224.

- [24] H. Yukawa, “On the Interaction of Elementary Particles I”, *Proc. Phys. Math. Soc. Jap.* **17** (1935) 48–57, doi:10.1143/PTPS.1.1. [Prog. Theor. Phys. Suppl.1,1(1935)].
- [25] S. H. Neddermeyer and C. D. Anderson, “Note on the Nature of Cosmic Ray Particles”, *Phys. Rev.* **51** (1937) 884–886, doi:10.1103/PhysRev.51.884.
- [26] C. M. G. Lattes, G. P. S. Occhialini, and C. F. Powell, “Observations on the Tracks of Slow Mesons in Photographic Emulsions. 1”, *Nature* **160** (1947) 453–456, doi:10.1038/160453a0.
- [27] C. L. Cowan and Reines, “Detection of the free neutrino: A Confirmation”, *Science* **124** (1956) 103, doi:10.1126/science.124.3212.103.
- [28] E. Fermi, “Fermi’s Theory of Beta Decay”, *Z. Phy.* **88** (1934) 161.
- [29] G. D. Rochester and C. C. Butler, “Evidence for the Existence of New Unstable Elementary Particles”, *Nature* **160** (1947) 855–857, doi:10.1038/160855a0.
- [30] V. D. Hopper and S. Biswas, “Evidence Concerning the Existence of the New Unstable Elementary Neutral Particle”, *Phys. Rev.* **80** (Dec, 1950) 1099, doi:10.1103/PhysRev.80.1099.
- [31] A. Bonetti, R. L. Setti, M. Panetti, and G. Tomasini, “On the existence of unstable charged particles of hyperprototic mass”, *Il Nuovo Cimento* **10** (1953) 1736–1743, doi:10.1007/BF02781667.
- [32] C. M. York, R. B. Leighton, and E. K. Bjornerud, “Direct Experimental Evidence for the Existence of a Heavy Positive *V* Particle”, *Phys. Rev.* **90** (1953) 167–168, doi:10.1103/PhysRev.90.167.
- [33] E. Cowan, “A *V*-Decay Event with a Heavy Negative Secondary, and Identification of the Secondary *V*-Decay Event in a Cascade”, *Physical Review* **94** (1954) 161.
- [34] V. E. Barnes et al., “Observation of a Hyperon with Strangeness -3”, *Phys. Rev. Lett.* **12** (1964) 204–206, doi:10.1103/PhysRevLett.12.204.
- [35] M. Gell-Mann, “A Schematic Model of Baryons and Mesons”, *Phys. Lett.* **8** (1964) 214–215, doi:10.1016/S0031-9163(64)92001-3.

- [36] G. Zweig, “An  $SU_3$  model for strong interaction symmetry and its breaking; Version 2”,. Version 1 is CERN preprint 8182/TH.401, Jan. 17, 1964.
- [37] Y. L. Dokshitzer, “Calculation of the structure functions for deep inelastic scattering and  $e^+ e^-$  annihilation by perturbation theory in quantum chromodynamics”, *Zh. Eksp. Teor. Fiz.* **73** (1977) 1216.
- [38] H. Fritzsch, M. Gell-Mann, and H. Leutwyler, “Advantages of the Color Octet Gluon Picture”, *Phys. Lett.* **47B** (1973) 365, doi:10.1016/0370-2693(73)90625-4.
- [39] TASSO Collaboration, “High energy trends in  $e^+e^-$  physics”, *Invited talk at Geneva Conference* (1979).
- [40] J. D. Bjorken and S. L. Glashow, “Elementary Particles and  $SU(4)$ ”, *Phys. Lett.* **11** (1964) 255–257, doi:10.1016/0031-9163(64)90433-0.
- [41] S. L. Glashow, J. Iliopoulos, and L. Maiani, “Weak Interactions with Lepton-Hadron Symmetry”, *Phys. Rev.* **D2** (1970) 1285–1292, doi:10.1103/PhysRevD.2.1285.
- [42] E598 Collaboration, “Experimental Observation of a Heavy Particle J”, *Phys. Rev. Lett.* **33** (1974) 1404–1406, doi:10.1103/PhysRevLett.33.1404.
- [43] SLAC-SP-017 Collaboration, “Discovery of a Narrow Resonance in  $e^+ e^-$  Annihilation”, *Phys. Rev. Lett.* **33** (1974) 1406–1408, doi:10.1103/PhysRevLett.33.1406. [Adv. Exp. Phys.5,141(1976)].
- [44] M. L. Perl et al., “Evidence for Anomalous Lepton Production in  $e^+e^-$  Annihilation”, *Phys. Rev. Lett.* **35** (1975) 1489–1492, doi:10.1103/PhysRevLett.35.1489.
- [45] S. W. Herb et al., “Observation of a Dimuon Resonance at 9.5-GeV in 400-GeV Proton-Nucleus Collisions”, *Phys. Rev. Lett.* **39** (1977) 252–255, doi:10.1103/PhysRevLett.39.252.
- [46] CDF Collaboration, “Observation of top quark production in  $\bar{p}p$  collisions”, *Phys. Rev. Lett.* **74** (1995) 2626–2631, doi:10.1103/PhysRevLett.74.2626, arXiv:hep-ex/9503002.

- [47] D0 Collaboration, “Observation of the top quark”, *Phys. Rev. Lett.* **74** (1995) 2632–2637, doi:10.1103/PhysRevLett.74.2632, arXiv:hep-ex/9503003.
- [48] T. D. Lee and C.-N. Yang, “Question of Parity Conservation in Weak Interactions”, *Phys. Rev.* **104** (1956) 254–258, doi:10.1103/PhysRev.104.254.
- [49] C. S. Wu et al., “Experimental Test of Parity Conservation in Beta Decay”, *Phys. Rev.* **105** (1957) 1413–1414, doi:10.1103/PhysRev.105.1413.
- [50] C.-N. Yang and R. L. Mills, “Conservation of Isotopic Spin and Isotopic Gauge Invariance”, *Phys. Rev.* **96** (1954) 191–195, doi:10.1103/PhysRev.96.191.
- [51] P. W. Higgs, “Broken symmetries, massless particles and gauge fields”, *Phys. Lett.* **12** (1964) 132–133, doi:10.1016/0031-9163(64)91136-9.
- [52] P. W. Higgs, “Broken Symmetries and the Masses of Gauge Bosons”, *Phys. Rev. Lett.* **13** (1964) 508–509, doi:10.1103/PhysRevLett.13.508.
- [53] P. W. Higgs, “Spontaneous Symmetry Breakdown without Massless Bosons”, *Phys. Rev.* **145** (1966) 1156–1163, doi:10.1103/PhysRev.145.1156.
- [54] F. Englert and R. Brout, “Broken Symmetry and the Mass of Gauge Vector Mesons”, *Phys. Rev. Lett.* **13** (1964) 321–323, doi:10.1103/PhysRevLett.13.321.
- [55] G. S. Guralnik, C. R. Hagen, and T. W. B. Kibble, “Global Conservation Laws and Massless Particles”, *Phys. Rev. Lett.* **13** (1964) 585–587, doi:10.1103/PhysRevLett.13.585.
- [56] Gargamelle Neutrino Collaboration, “Observation of Neutrino Like Interactions Without Muon Or Electron in the Gargamelle Neutrino Experiment”, *Phys. Lett.* **B46** (1973) 138–140, doi:10.1016/0370-2693(73)90499-1.
- [57] UA1 Collaboration, “Experimental Observation of Isolated Large Transverse Energy Electrons with Associated Missing Energy at  $\sqrt{s} = 540$  GeV”, *Phys. Lett.* **B122** (1983) 103–116, doi:10.1016/0370-2693(83)91177-2.

- [58] UA2 Collaboration, “Observation of Single Isolated Electrons of High Transverse Momentum in Events with Missing Transverse Energy at the CERN  $p\bar{p}$  Collider”, *Phys. Lett.* **B122** (1983) 476–485, doi:10.1016/0370-2693(83)91605-2.
- [59] UA1 Collaboration, “Experimental Observation of Lepton Pairs of Invariant Mass Around 95-GeV/c<sup>2</sup> at the CERN SPS Collider”, *Phys. Lett.* **B126** (1983) 398–410, doi:10.1016/0370-2693(83)90188-0.
- [60] UA1 Collaboration, “Further Evidence for Charged Intermediate Vector Bosons at the SPS Collider”, *Phys. Lett.* **B129** (1983) 273–282, doi:10.1016/0370-2693(83)90860-2.
- [61] UA2 Collaboration, “Evidence for  $Z^0 \rightarrow e^+e^-$  at the CERN  $p\bar{p}$  Collider”, *Phys. Lett.* **B129** (1983) 130–140, doi:10.1016/0370-2693(83)90744-X.
- [62] ATLAS Collaboration, “Observation of a new particle in the search for the Standard Model Higgs boson with the ATLAS detector at the LHC”, *Phys. Lett.* **B716** (2012) 1–29, doi:10.1016/j.physletb.2012.08.020, arXiv:1207.7214.
- [63] CMS Collaboration, “Observation of a new boson at a mass of 125 GeV with the CMS experiment at the LHC”, *Phys. Lett.* **B716** (2012) 30–61, doi:10.1016/j.physletb.2012.08.021, arXiv:1207.7235.
- [64] CMS Collaboration, “Combination of standard model Higgs boson searches and measurements of the properties of the new boson with a mass near 125 GeV”, (2013). CMS-PAS-HIG-13-005.
- [65] ATLAS Collaboration, “Updated coupling measurements of the Higgs boson with the ATLAS detector using up to 25 fb<sup>-1</sup> of proton-proton collision data”, (2014). ATLAS-CONF-2014-009.
- [66] Super-Kamiokande Collaboration, “Evidence for oscillation of atmospheric neutrinos”, *Phys. Rev. Lett.* **81** (1998) 1562–1567, doi:10.1103/PhysRevLett.81.1562, arXiv:hep-ex/9807003.
- [67] Super-Kamiokande Collaboration, “Constraints on neutrino oscillations using 1258 days of Super-Kamiokande solar neutrino data”, *Phys. Rev. Lett.* **86** (2001) 5656–5660, doi:10.1103/PhysRevLett.86.5656, arXiv:hep-ex/0103033.

- [68] SNO Collaboration, “Direct evidence for neutrino flavor transformation from neutral current interactions in the Sudbury Neutrino Observatory”, *Phys. Rev. Lett.* **89** (2002) 011301, doi:10.1103/PhysRevLett.89.011301, arXiv:nucl-ex/0204008.
- [69] KamLAND Collaboration, “Measurement of neutrino oscillation with KamLAND: Evidence of spectral distortion”, *Phys. Rev. Lett.* **94** (2005) 081801, doi:10.1103/PhysRevLett.94.081801, arXiv:hep-ex/0406035.
- [70] K2K Collaboration, “Evidence for muon neutrino oscillation in an accelerator-based experiment”, *Phys. Rev. Lett.* **94** (2005) 081802, doi:10.1103/PhysRevLett.94.081802, arXiv:hep-ex/0411038.
- [71] MINOS Collaboration, “Observation of muon neutrino disappearance with the MINOS detectors and the NuMI neutrino beam”, *Phys. Rev. Lett.* **97** (2006) 191801, doi:10.1103/PhysRevLett.97.191801, arXiv:hep-ex/0607088.
- [72] Particle Data Group Collaboration, “Review of Particle Physics”, *Chin. Phys. C* **38** (2014) 090001, doi:10.1088/1674-1137/38/9/090001.
- [73] F. J. Dyson, “The Radiation theories of Tomonaga, Schwinger, and Feynman”, *Phys. Rev.* **75** (1949) 486–502, doi:10.1103/PhysRev.75.486.
- [74] M. E. Peskin and D. V. Schroeder, “An Introduction to quantum field theory”. Addison-Wesley (1995) 842 p, Reading, USA, 1995.
- [75] S. Kluth, “Review of alpha(s) Measurements”, *Conf. Proc. C060726* (2006) 449–452, arXiv:hep-ex/0609020. [,449(2006)].
- [76] D. J. Gross and F. Wilczek, “Asymptotically Free Gauge Theories. 1”, *Phys. Rev. D* **8** (1973) 3633–3652, doi:10.1103/PhysRevD.8.3633.
- [77] D. J. Gross and F. Wilczek, “Asymptotically Free Gauge Theories. 2.”, *Phys. Rev. D* **9** (1974) 980–993, doi:10.1103/PhysRevD.9.980.
- [78] H. D. Politzer, “Asymptotic Freedom: An Approach to Strong Interactions”, *Phys. Rept.* **14** (1974) 129–180, doi:10.1016/0370-1573(74)90014-3.
- [79] M. Goldhaber, L. Grodzins, and A. W. Sunyar, “Helicity of Neutrinos”, *Phys. Rev. D* **109** (1958) 1015, doi:10.1103/PhysRev.109.1015.

- [80] T. Nakano and K. Nishijima, “Charge Independence for V-particles”, *Prog. Theor. Phys.* **10** (1953) 581, doi:10.1143/PTP.10.581.
- [81] K. Nishijima and Kazuhiko, “Charge Independence Theory of V Particles”, *Prog. Theor. Phys.* **13** (1955) 285, doi:10.1143/PTP.13.285.
- [82] M. Gell-Mann, “The interpretation of the new particles as displaced charge multiplets”, *Nuovo Cim.* **4** (1956) 848, doi:10.1007/BF02748000.
- [83] A. Djouadi, “The Anatomy of electro-weak symmetry breaking. I: The Higgs boson in the standard model”, *Phys. Rept.* **457** (2008) 1, doi:10.1016/j.physrep.2007.10.004, arXiv:hep-ph/0503172.
- [84] J. C. Pati, A. Salam, and J. A. Strathdee, “Are Quarks Composite?”, *Phys. Lett.* **B59** (1975) 265, doi:10.1016/0370-2693(75)90042-8.
- [85] E. Eichten, K. D. Lane, and M. E. Peskin, “New Tests for Quark and Lepton Substructure”, *Phys. Rev. Lett.* **50** (1983) 811, doi:10.1103/PhysRevLett.50.811.
- [86] U. Baur, I. Hinchliffe, and D. Zeppenfeld, “Excited Quark Production at Hadron Colliders”, *Int.J.Mod.Phys.* **A2** (1987) 1285, doi:10.1142/S0217751X87000661.
- [87] U. Baur, M. Spira, and P. Zerwas, “Excited Quark and Lepton Production at Hadron Colliders”, *Phys.Rev.* **D42** (1990) 815, doi:10.1103/PhysRevD.42.815.
- [88] ZEUS Collaboration, “A Search for excited fermions in  $e^+p$  collisions at HERA”, *Z. Phys.* **C76** (1997) 631, doi:10.1007/s002880050585, arXiv:hep-ex/9708007.
- [89] CDF Collaboration, “Search for excited quarks in  $p\bar{p}$  collisions at  $\sqrt{s} = 1.8$  TeV”, *Phys.Rev.Lett.* **72** (1994) 3004, doi:10.1103/PhysRevLett.72.3004.
- [90] CDF Collaboration, “Search for new particles decaying to dijets at CDF”, *Phys.Rev.* **D55** (1997) 5263, doi:10.1103/PhysRevD.55.R5263, arXiv:hep-ex/9702004.
- [91] D0 Collaboration Collaboration, “Search for new particles in the two jet decay channel with the D0 detector”, *Phys.Rev.* **D69** (2004) 111101, doi:10.1103/PhysRevD.69.111101, arXiv:hep-ex/0308033.

- [92] ATLAS Collaboration, “Search for new phenomena in dijet mass and angular distributions from  $pp$  collisions at  $\sqrt{s} = 13$  TeV with the ATLAS detector”, *Phys. Lett.* **B754** (2016) 302, doi:10.1016/j.physletb.2016.01.032, arXiv:1512.01530.
- [93] ATLAS Collaboration, “Search for new phenomena with photon+jet events in proton-proton collisions at  $\sqrt{s} = 13$  TeV with the ATLAS detector”, *JHEP* **03** (2016) 041, doi:10.1007/JHEP03(2016)041, arXiv:1512.05910.
- [94] CMS Collaboration, “Search for narrow resonances decaying to dijets in proton-proton collisions at  $\sqrt(s) = 13$  TeV”, *Phys. Rev. Lett.* **116** (2016), no. 7, 071801, doi:10.1103/PhysRevLett.116.071801, arXiv:1512.01224.
- [95] ATLAS Collaboration, “Search for single  $b^*$ -quark production with the ATLAS detector at  $\sqrt{s} = 7$  TeV”, *Phys. Lett.* **B721** (2013) 171, doi:10.1016/j.physletb.2013.03.016, arXiv:1301.1583.
- [96] CMS Collaboration, “Search for the production of an excited bottom quark decaying to  $tW$  in proton-proton collisions at  $\sqrt{s} = 8$  TeV”, *JHEP* **01** (2016) 166, doi:10.1007/JHEP01(2016)166, arXiv:1509.08141.
- [97] CMS Collaboration, “Search for resonances and quantum black holes using dijet mass spectra in proton-proton collisions at  $\sqrt{s} = 8$  TeV”, *Phys. Rev.* **D91** (2015) 052009, doi:10.1103/PhysRevD.91.052009, arXiv:1501.04198.
- [98] D. S. Gorbunov and V. A. Rubakov, “Introduction to the theory of the early universe: Hot big bang theory”. World Scientific, Hackensack, 2011.
- [99] O. S. Brüning et al., “LHC Design Report”. CERN, Geneva, 2004. CERN-2004-003-V-1.
- [100] L. Evans and P. Bryant, “LHC Machine”, *JINST* **3** (2008) S08001, doi:10.1088/1748-0221/3/08/S08001.
- [101] S. Myers and E. Picasso, “The design, construction and commissioning of the CERN large Electron–Positron collider”, *Contemporary Physics* **31** (1990) 387, doi:10.1080/00107519008213789.

- [102] S. Holmes, R. S. Moore, and V. Shiltsev, “Overview of the Tevatron Collider Complex: Goals, Operations and Performance”, *JINST* **6** (2011) T08001, doi:10.1088/1748-0221/6/08/T08001, arXiv:1106.0909.
- [103] ATLAS Collaboration, A. Airapetian et al., “ATLAS detector and physics performance: Technical Design Report, 1”. TDR ATLAS. CERN, Geneva, 1999. ATLAS-TDR-014; CERN-LHCC-99-014.
- [104] CMS Collaboration, G. L. Bayatian et al., “CMS Physics: Technical Design Report Volume 1: Detector Performance and Software”. TDR CMS. CERN, Geneva, 2006. CERN-LHCC-2006-001.
- [105] ALICE Collaboration, P. Cortese et al., “ALICE physics performance: Technical Design Report”. TDR ALICE. CERN, Geneva, 2005. ALICE-TDR-13; CERN-LHCC-2005-030.
- [106] LHCb Collaboration, R. Antunes-Nobrega et al., “LHCb reoptimized detector design and performance: Technical Design Report”. TDR LHCb. CERN, Geneva, 2003. LHCb-TDR-9; CERN-LHCC-2003-030.
- [107] “CERN Experiments and Facilities”. <http://home.web.cern.ch/about>. Accessed, 2015.
- [108] CMS Collaboration, S. Chatrchyan et al., “CMS Luminosity - Public Results”. <https://twiki.cern.ch/twiki/bin/view/CMSPublic/LumiPublicResults>. Accessed: 2014-09-30.
- [109] CMS Collaboration, “The CMS experiment at the CERN LHC”, *JINST* **3** (2008) S08004, doi:10.1088/1748-0221/3/08/S08004.
- [110] CMS Collaboration, V. Karimäki et al., “The CMS tracker system project: Technical Design Report”. Technical Design Report CMS. CERN, Geneva, 1997.
- [111] CMS Collaboration, “Description and performance of track and primary-vertex reconstruction with the CMS tracker”, *JINST* **9** (2014) P10009, doi:10.1088/1748-0221/9/10/P10009, arXiv:1405.6569.
- [112] CMS Collaboration, “Studies of Tracker Material”, (2010). CMS-PAS-TRK-10-003.

- [113] R. Baur and W. H. Bertl, “The CMS pixel vertex detector”, *Nucl. Phys. Proc. Suppl.* **78** (1999) 293, doi:10.1016/S0920-5632(99)00560-5.
- [114] CMS Collaboration, M. Dominguez et al., “CMS Technical Design Report for the Pixel Detector Upgrade”. Technical Design Report CMS. CERN, Geneva, 2012.
- [115] CMS Collaboration, “Upgrade of the CMS tracker”, *JINST* **9** (2014) C03041, doi:10.1088/1748-0221/9/03/C03041.
- [116] CMS Collaboration, “The CMS electromagnetic calorimeter project: Technical Design Report”. TDR CMS. CERN, Geneva, 1997. CERN-LHCC-97-033.
- [117] CMS Collaboration, “Energy Calibration and Resolution of the CMS Electromagnetic Calorimeter in  $pp$  Collisions at  $\sqrt{s} = 7$  TeV”, *JINST* **8** (2013) P09009, doi:10.1088/1748-0221/8/09/P09009, arXiv:1306.2016.
- [118] R. Wigmans, “Advances in hadron calorimetry”, *Ann. Rev. Nucl. Part. Sci.* **41** (1991) 133, doi:10.1146/annurev.ns.41.120191.001025.
- [119] CMS Collaboration, “The CMS hadron calorimeter project: Technical Design Report”. TDR CMS. CERN, Geneva, 1997. CERN-LHCC-97-031.
- [120] CMS HCAL Collaboration, “Design, performance, and calibration of CMS hadron-barrel calorimeter wedges”, *Eur.Phys.J.* **C55** (2008) 159–171, doi:10.1140/epjc/s10052-008-0573-y.
- [121] CMS HCAL Collaboration, “Design, performance, and calibration of CMS hadron endcap calorimeters”, (2008). CERN-CMS-NOTE-2008-010.
- [122] G. Bayatian et al., “Design, performance and calibration of the CMS forward calorimeter wedges”, *Eur.Phys.J.* **C53** (2008) 139–166, doi:10.1140/epjc/s10052-007-0459-4.
- [123] CMS HCAL Collaboration, “Design, performance, and calibration of the CMS Hadron-outer calorimeter”, *Eur.Phys.J.* **C57** (2008) 653–663, doi:10.1140/epjc/s10052-008-0756-6.
- [124] CMS Collaboration, “The CMS magnet project: Technical Design Report”. Technical Design Report CMS. CERN, Geneva, 1997.

- [125] CMS Collaboration, “The CMS muon project: Technical Design Report”. TDR CMS. CERN, Geneva, 1997. CERN-LHCC-97-032.
- [126] CMS Collaboration, G. L. Bayatyan et al., “CMS TriDAS project: Technical Design Report, Volume 1: The Trigger Systems”. TDR CMS. CERN, Geneva, 2000. CMS-TDR-6-1; CERN-LHCC-2000-038.
- [127] CMS Collaboration, S. Cittolin et al., “CMS The TriDAS Project: Technical Design Report, Volume 2: Data Acquisition and High-Level Trigger. CMS trigger and data-acquisition project”. TDR CMS. CERN, Geneva, 2002. CMS-TDR-6; CERN-LHCC-2002-026.
- [128] C. Eck et al., “LHC computing Grid: Technical Design Report. Version 1.06 (20 Jun 2005)”. Technical Design Report LCG. CERN, Geneva, 2005.
- [129] M. Giffels et al., “The CMS Data Management System”, *J. Phys. Conf. Ser.* **513** (2014) 042052, doi:10.1088/1742-6596/513/4/042052.
- [130] R. Egeland, T. Wildish, and S. Metson, “Data transfer infrastructure for CMS data taking”, *Proceedings of Science ACAT08* (2008) 033.
- [131] R. Egeland, T. Wildish, and C.-H. Huang, “PhEDEx Data Service”, Technical Report CMS-CR-2009-071, CERN, Geneva, (2009).  
<https://cds.cern.ch/record/1196164>.
- [132] CMS Collaboration, “The CMS dataset bookkeeping service”, *J. Phys. Conf. Ser.* **119** (2008) 072001, doi:10.1088/1742-6596/119/7/072001.
- [133] V. Kuznetsov, D. Evans, and S. Metson, “The CMS data aggregation system”, *Procedia Computer Science* **1** (2010) 1535, doi:10.1016/j.procs.2010.04.172.
- [134] R. Brun and F. Rademakers, “ROOT: An object oriented data analysis framework”, *Nucl. Instrum. Meth.* **A389** (1997) 81, doi:10.1016/S0168-9002(97)00048-X.
- [135] CMS Collaboration, “The CMS reconstruction software”, *J.Phys.Conf.Ser.* **331** (2011) 032020, doi:10.1088/1742-6596/331/3/032020.
- [136] A. Buckley et al., “General-purpose event generators for LHC physics”, *Phys. Rept.* **504** (2011) 145–233, doi:10.1016/j.physrep.2011.03.005, arXiv:1101.2599.

- [137] M. Dobbs et al., “Les Houches guidebook to Monte Carlo generators for hadron collider physics”, [arXiv:hep-ph/0403045](https://arxiv.org/abs/hep-ph/0403045).
- [138] C. P. Robert, “Monte Carlo Methods”. Wiley Online Library, 2004.
- [139] C. P. Robert, “Monte Carlo Methods”,  
[doi:10.1002/9781118445112.stat03876.pub2](https://doi.org/10.1002/9781118445112.stat03876.pub2).
- [140] CMS Collaboration, “Particle-flow reconstruction and global event description with the CMS detector”, *JINST* **12** (2017) P10003,  
[doi:10.1088/1748-0221/12/10/P10003](https://doi.org/10.1088/1748-0221/12/10/P10003), [arXiv:1706.04965](https://arxiv.org/abs/1706.04965).
- [141] CMS Collaboration, “Track Reconstruction in the CMS tracker”, Technical Report CMS-NOTE-2006-041, CERN, Geneva, (2006).  
<https://cds.cern.ch/record/934067>.
- [142] R. Frühwirth, “Application of Kalman filtering to track and vertex fitting”, *Nucl. Instrum. Meth.* **A262** (1987) 444–450,  
[doi:10.1016/0168-9002\(87\)90887-4](https://doi.org/10.1016/0168-9002(87)90887-4).
- [143] P. Billoir, “Progressive track recognition with a Kalman like fitting procedure”, *Comput. Phys. Commun.* **57** (1989) 390–394,  
[doi:10.1016/0010-4655\(89\)90249-X](https://doi.org/10.1016/0010-4655(89)90249-X).
- [144] P. Billoir and S. Qian, “Simultaneous pattern recognition and track fitting by the Kalman filtering method”, *Nucl. Instrum. Meth.* **A294** (1990) 219,  
[doi:10.1016/0168-9002\(90\)91835-Y](https://doi.org/10.1016/0168-9002(90)91835-Y).
- [145] CMS Collaboration, “Beam Position Determination using Tracks”, Technical Report CMS-NOTE-2007-021, CERN, Geneva, (2007).  
<https://cds.cern.ch/record/1061285>.
- [146] K. Rose, “Deterministic Annealing for Clustering, Compression, Classification, Regression, and Related Optimization Problems”, *Proceedings of the IEEE* **86** (1998) doi:10.1109/5.726788.
- [147] CMS Collaboration, “Performance of photon reconstruction and identification with the CMS detector in proton-proton collisions at  $\sqrt{s} = 8$  TeV”, [arXiv:1502.02702](https://arxiv.org/abs/1502.02702).
- [148] CMS Collaboration, “Review of clustering algorithms and energy corrections in ECAL”, technical report, CERN, Geneva, (2010).  
<https://cds.cern.ch/record/1365024>.

- [149] E. Meschi, T. Monteiro, C. Seez, and P. Vikas, “Electron Reconstruction in the CMS Electromagnetic Calorimeter”, Technical Report CMS-NOTE-2001-034, CERN, Geneva, (2001).  
<https://cds.cern.ch/record/687345>.
- [150] S. Catani, Y. L. Dokshitzer, M. Seymour, and B. Webber, “Longitudinally invariant  $k_t$  clustering algorithms for hadron hadron collisions”, *Nucl.Phys.* **B406** (1993) 187, doi:10.1016/0550-3213(93)90166-M.
- [151] M. Cacciari, G. P. Salam, and G. Soyez, “The Anti- $k_t$  jet clustering algorithm”, *JHEP* **0804** (2008) 063,  
doi:10.1088/1126-6708/2008/04/063, arXiv:0802.1189.
- [152] CMS Collaboration, “A Cambridge-Aachen (C-A) based Jet Algorithm for boosted top-jet tagging”, Technical Report CMS-PAS-JME-09-001, CERN, Geneva, (2009). <http://cds.cern.ch/record/1194489>.
- [153] Y. L. Dokshitzer, G. Leder, S. Moretti, and B. Webber, “Better jet clustering algorithms”, *JHEP* **9708** (1997) 001,  
doi:10.1088/1126-6708/1997/08/001, arXiv:hep-ph/9707323.
- [154] CMS Collaboration, “Particle-Flow Event Reconstruction in CMS and Performance for Jets, Taus, and MET”, Technical Report CMS-PAS-PFT-09-001, CERN, Geneva, (2009).  
<https://cds.cern.ch/record/1194487>.
- [155] CMS Collaboration, “Plans for Jet Energy Corrections at CMS”, Technical Report CMS-PAS-JME-07-002, CERN, 2008. Geneva, (2008).  
<https://cds.cern.ch/record/1194485>.
- [156] M. Cacciari and G. P. Salam, “Pileup subtraction using jet areas”, *Phys.Lett.* **B659** (2008) 119, doi:10.1016/j.physletb.2007.09.077, arXiv:0707.1378.
- [157] CMS Collaboration, “Identification of b-quark jets with the CMS experiment”, *JINST* **8** (2013) P04013,  
doi:10.1088/1748-0221/8/04/P04013, arXiv:1211.4462.
- [158] CMS Collaboration, “Identification of heavy-flavour jets with the CMS detector in pp collisions at 13 TeV”, (2017). arXiv:1712.07158. Submitted to *JINST*.

- [159] CMS Collaboration, “Jet Identification in the CMS detector”.  
<https://twiki.cern.ch/twiki/bin/viewauth/CMS/JetID>. Accessed: 2016.
- [160] J. Shiers, “The Worldwide LHC Computing Grid (worldwide LCG)”, *Computer Physics Communications* **177** (2007) 219, doi:10.1016/j.cpc.2007.02.021. Proceedings of the Conference on Computational Physics 2006.
- [161] A. Martin, W. Stirling, R. Thorne, and G. Watt, “Parton distributions for the LHC”, *Eur.Phys.J.* **C63** (2009) 189–285, doi:10.1140/epjc/s10052-009-1072-5, arXiv:0901.0002.
- [162] T. Sjöstrand et al., “An Introduction to PYTHIA 8.2”, *Comput. Phys. Commun.* **191** (2015) 159, doi:10.1016/j.cpc.2015.01.024, arXiv:1410.3012.
- [163] J. Alwall et al., “The automated computation of tree-level and next-to-leading order differential cross sections, and their matching to parton shower simulations”, *JHEP* **1407** (2014) 079, doi:10.1007/JHEP07(2014)079, arXiv:1405.0301.
- [164] M. Bahr et al., “Herwig++ Physics and Manual”, *Eur.Phys.J.* **C58** (2008) 639–707, doi:10.1140/epjc/s10052-008-0798-9, arXiv:0803.0883.
- [165] M. L. Mangano et al., “ALPGEN, a generator for hard multiparton processes in hadronic collisions”, *JHEP* **0307** (2003) 001, doi:10.1088/1126-6708/2003/07/001, arXiv:hep-ph/0206293.
- [166] T. Gleisberg et al., “Event generation with SHERPA 1.1”, *JHEP* **0902** (2009) 007, doi:10.1088/1126-6708/2009/02/007, arXiv:0811.4622.
- [167] T. Sjöstrand and M. Bengtsson, “The Lund Monte Carlo for Jet Fragmentation and e+ e- Physics. Jetset Version 6.3: An Update”, *Comput. Phys. Commun.* **43** (1987) 367, doi:10.1016/0010-4655(87)90054-3.
- [168] P. de Aquino et al., “ALOHA: Automatic Libraries Of Helicity Amplitudes for Feynman Diagram Computations”, *Comput. Phys. Commun.* **183** (2012) 2254–2263, doi:10.1016/j.cpc.2012.05.004, arXiv:1108.2041.

- [169] J. Alwall et al., “A Standard format for Les Houches event files”, *Comput.Phys.Commun.* **176** (2007) 300–304, doi:10.1016/j.cpc.2006.11.010, arXiv:hep-ph/0609017.
- [170] F. Krauss, “Matrix elements and parton showers in hadronic interactions”, *JHEP* **0208** (2002) 015, doi:10.1088/1126-6708/2002/08/015, arXiv:hep-ph/0205283.
- [171] M. L. Mangano, M. Moretti, and R. Pittau, “Multijet matrix elements and shower evolution in hadronic collisions:  $Wb\bar{b} + n$  jets as a case study”, *Nucl.Phys.* **B632** (2002) 343–362, doi:10.1016/S0550-3213(02)00249-3, arXiv:hep-ph/0108069.
- [172] GEANT4 Collaboration, “GEANT4 — a simulation toolkit”, *Nucl. Instrum. Meth. A* **506** (2003) 250, doi:10.1016/S0168-9002(03)01368-8.
- [173] CMS Collaboration, “CRAB: Distributed analysis tool for CMS”, Technical Report CMS-CR-2009-318, CERN, Geneva, (2009).  
<https://cds.cern.ch/record/1358821>.
- [174] CMS Collaboration, “Event generator tunes obtained from underlying event and multiparton scattering measurements”, *Eur. Phys. J. C* **76** (2016) 155, doi:10.1140/epjc/s10052-016-3988-x, arXiv:1512.00815.
- [175] P. Skands, S. Carrazza, and J. Rojo, “Tuning PYTHIA 8.1: the Monash 2013 Tune”, *Eur. Phys. J. C* **74** (2014) 3024, doi:10.1140/epjc/s10052-014-3024-y, arXiv:1404.5630.
- [176] R. D. Ball et al., “Parton distributions with LHC data”, *Nucl. Phys. B* **867** (2013) 244, doi:10.1016/j.nuclphysb.2012.10.003, arXiv:1207.1303.
- [177] J. Alwall et al., “Comparative study of various algorithms for the merging of parton showers and matrix elements in hadronic collisions”, *Eur. Phys. J. C* **53** (2008) 473, doi:10.1140/epjc/s10052-007-0490-5, arXiv:0706.2569.
- [178] CMS Collaboration, S. Chatrchyan et al., “Pile-up scenario for Run-II”.  
<https://twiki.cern.ch/twiki/bin/view/CMS/PdmVPileUpDescription>,  
[https://twiki.cern.ch/twiki/bin/viewauth/CMS/PileupJSONFileforData#Pileup\\_JSON\\_Files\\_For\\_Run\\_II](https://twiki.cern.ch/twiki/bin/viewauth/CMS/PileupJSONFileforData#Pileup_JSON_Files_For_Run_II).

- [179] M. Cacciari, G. P. Salam, and G. Soyez, “FastJet User Manual”, *Eur. Phys. J. C* **72** (2012) 1896, doi:10.1140/epjc/s10052-012-1896-2, arXiv:1111.6097.
- [180] CMS Collaboration, S. Chatrchyan et al., “B-tag Recommendation”. <https://twiki.cern.ch/twiki/bin/viewauth/CMS/BtagRecommendation80X>.
- [181] CMS Collaboration, S. Chatrchyan et al., “B-tag Calibration”. <https://twiki.cern.ch/twiki/bin/view/CMS/BTagCalibration>.
- [182] S. D. Ellis, Z. Kunszt, and D. E. Soper, “Two jet production in hadron collisions at order  $\alpha_s^3$  in QCD”, *Phys.Rev.Lett.* **69** (1992) 1496–1499, doi:10.1103/PhysRevLett.69.1496.
- [183] W. Giele, E. N. Glover, and D. A. Kosower, “Higher order corrections to jet cross-sections in hadron colliders”, *Nucl.Phys. B* **403** (1993) 633–670, doi:10.1016/0550-3213(93)90365-V, arXiv:hep-ph/9302225.
- [184] CMS Collaboration, S. Chatrchyan et al., “Physics Analysis Oriented Event Display”. <https://twiki.cern.ch/twiki/bin/view/CMS/WorkBookFireworks>. Accessed: 2015.
- [185] S. Ozturk et al., “Plans to Search for New Particles Decaying to Dijets in  $pp$  Collisions at  $\sqrt{s} = 10$  TeV”, (2009). CMS AN-2009/070.
- [186] CDF Collaboration, “Search for new particles decaying into dijets in proton-antiproton collisions at  $\sqrt{s} = 1.96$  TeV”, *Phys. Rev. D* **79** (2009) 112002, doi:10.1103/PhysRevD.79.112002, arXiv:0812.4036.
- [187] R. M. Harris and K. Kousouris, “Searches for Dijet Resonances at Hadron Colliders”, *Int. J. Mod. Phys. A* **26** (2011) 5005, doi:10.1142/S0217751X11054905, arXiv:1110.5302.
- [188] ATLAS Collaboration, “Search for production of resonant states in the photon-jet mass distribution using  $pp$  collisions at  $\sqrt{s} = 7$  TeV collected by the ATLAS detector”, *Phys. Rev. Lett.* **108** (2012) 211802, doi:10.1103/PhysRevLett.108.211802, arXiv:1112.3580.
- [189] CMS Collaboration, “Search for narrow resonances using the dijet mass spectrum in  $pp$  collisions at  $\sqrt{s} = 8$  TeV”, *Phys. Rev. D* **87** (2013) 114015, doi:10.1103/PhysRevD.87.114015, arXiv:1302.4794.

- [190] ATLAS Collaboration, “Search for new phenomena in photon+jet events collected in proton–proton collisions at  $\sqrt{s} = 8$  TeV with the ATLAS detector”, *Phys. Lett.* **B728** (2014) 562, doi:10.1016/j.physletb.2013.12.029, arXiv:1309.3230.
- [191] CMS Collaboration, “Search for excited quarks in the  $\gamma$ +jet final state in proton proton collisions at  $\sqrt{s} = 8$  TeV”, *Phys. Lett.* **B738** (2014) 274, doi:10.1016/j.physletb.2014.09.048, arXiv:1406.5171.
- [192] S. Baker and R. D. Cousins, “Clarification of the Use of Chi Square and Likelihood Functions in Fits to Histograms”, *Nucl. Instrum. Meth.* **221** (1984) 437–442, doi:10.1016/0167-5087(84)90016-4.
- [193] P. D. G. Collaboration, “Review of Particle Physics”, *Chin. Phys.* **C40** (2016) no. 10, 100001, doi:10.1088/1674-1137/40/10/100001.
- [194] CMS Collaboration, “Determination of Jet Energy Calibration and Transverse Momentum Resolution in CMS”, *JINST* **6** (2011) P11002, doi:10.1088/1748-0221/6/11/P11002, arXiv:1107.4277.
- [195] The ATLAS Collaboration, The CMS Collaboration, The LHC Higgs Combination Group Collaboration, “Procedure for the LHC Higgs boson search combination in Summer 2011”, Technical Report CMS-NOTE-2011-005. ATL-PHYS-PUB-2011-11, CERN, Geneva, (Aug, 2011). <https://cds.cern.ch/record/1379837>.
- [196] T. Junk, “Confidence level computation for combining searches with small statistics”, *Nucl. Instrum. Meth. A* **434** (1999) 435, doi:10.1016/S0168-9002(99)00498-2, arXiv:hep-ex/9902006.
- [197] A. L. Read, “Presentation of search results: The  $CL_s$  technique”, *J. Phys. G* **28** (2002) 2693, doi:10.1088/0954-3899/28/10/313.
- [198] G. Cowan, K. Cranmer, E. Gross, and O. Vitells, “Asymptotic formulae for likelihood-based tests of new physics”, *Eur. Phys. J. C* **71** (2011) 1554, doi:10.1140/epjc/s10052-011-1554-0, arXiv:1007.1727. [Erratum: *Eur. Phys. J. C* **73** (2013) 2501, 10.1140/epjc/s10052-013-2501-z].
- [199] I. Asimov, “Isaac Asimov: The Complete Stories, Vol. 1”. Broadway Books, New York City, USA, 1990.